Measurement of $\Gamma(D_s^+ \to \mu^+\nu)/\Gamma(D_s^+ \to \phi\pi^+)$ and the Pseudoscalar Decay Constant f_{D_S}

by

WEIPIN HE
B.S., Peking University, Beijing, 1990

DISSERTATION

Submitted in partial fulfillment of the requirements
for the degree of Doctor of Philosophy in Physics
in the Graduate School of Syracuse University

Approved ______________________
Professor Sheldon Stone

Date ______________________

October, 1998

ABSTRACT

In this thesis we present a new determination of f_{D_s} using 5 million $e^+e^- \to c\bar{c}$ events obtained with the CLEO II detector at the Cornell Electron Storage Ring (CESR). Our value is derived from our new measured ratio $\Gamma(D_s^+ \to \mu^+\nu)/\Gamma(D_s^+ \to \phi\pi^+) = 0.173 \pm 0.023 \pm 0.035$. Using $\mathcal{B}(D_s^+ \to \phi\pi^+) = (3.6 \pm 0.9)\%$, we extract $f_{D_s} = (280 \pm 19 \pm 28 \pm 34)$ MeV. We compare this result with various model calculations.

To My Parents

Committee Approval Page

ACKNOWLEDGMENTS

First I would like to thank my thesis advisor, Prof. Sheldon Stone for his constant attention, guidance and support. His mastery and deep insights of B and Charm physics, extensive experience working with the CLEO II detector, and knowledge of detector technology in general, make this analysis work possible.

I also thank my thesis committee members: Prof. Marina Artuso, Prof. Carol Rosenzweig, Prof. Joseph Schechter, Prof. Simon Catterall and Prof. Watson Lees(chair). Prof. Marina Artuso is leading the critical RICH electronics effort which uses advanced analog microchip technology to readout large number of RICH channels.

Prof. Tomasz Skwarnicki is remembered for teaching me how to do data analysis by reconstructing π^0 events when I first joined the group. His strong contribution to CLEO data analysis impressed me very much.

I thank Franz Muheim for his creative efforts in the original analysis, and his continuing helpful comments for the current analysis.

I express my gratitude to all the CLEO members, who designed, constructed and maintained the operation of the excellent CLEO II detector, where the data of the analysis comes from. And I gratefully acknowledge the effort of the CESR staff in providing us with excellent luminosity and running conditions.

I thank Prof. Giancarlo Moneti for reviewing the manuscript of this work.

Over the years, I have got a lot of help from Prof. Nahmin Horwitz, Prof. Giancarlo Moneti, Dr.Guosheng Zhu, and Dr.Yurii Mukhin and my best friends Dr. Xing Xia and Mr. Min Gao.

I would also like to thank my former colleagues in the Syracuse High Energy Group, with whom I worked with in the RICH project. Dr. Ray Mountain, Dr. Sacha Kopp, Dr. Georg Viehhauser and Silvia Schuh. You were fun to work with.

Finally, I give my special thanks to my parents and my brother in China.

Contents

List of Tables

List of Figures

Chapter 1

The Physics of Meson Decay Constant f_P

1.1 Introduction

One major goal of heavy flavor particle physics today is to measure the CKM matrix element parameters with precision, since it is the Standard Model's prescription for CP Violation. These measurements will allow a fundamental understanding of the matter-antimatter asymmetry in the known universe and provide critical tests for the Standard Model.

Measuring purely leptonic decays of heavy mesons allows the direct determination of meson decay constants, which connect measured quantities, such as the $B\bar{B}$ mixing ratio, to CKM matrix elements and other interesting physics quantities. Currently, it is not possible to determine f_B experimentally from leptonic B decays, so theoretical calculations of f_B must be used. The model dependent uncertainties associated with these calculations are large and they are the main sources of error in extracting the CKM matrix elements. Measurements of the Cabibbo-favored pseudoscalar decay constants such as f_{D_s} provide a check on these calculations and help discriminate among different models and calibrate their calculations.

We present in this document a new determination of f_{D_s} using 5 million $e^+e^- \to c\overline{c}$

events obtained with the CLEO II detector at the Cornell Electron Storage Ring (CESR). Our value is derived from our new measured ratio $\Gamma(D_s^+ \to \mu^+\nu)/\Gamma(D_s^+ \to \phi\pi^+) = 0.173 \pm 0.023 \pm 0.035$. Using $\mathcal{B}(D_s^+ \to \phi\pi^+) = (3.6 \pm 0.9)\%$, we extract $f_{D_s} = (280 \pm 19 \pm 28 \pm 34)$ MeV.

This document is divided into four parts: In Chapter 1, we give brief introduction to the physics motivation behind decay constants measurement, including Standard Model and CKM matrix and the important role played by decay constants in extracting CKM matrix elements. In Chapter 2, we will describe the experimental apparatus, which consists of the Cornell Electron Storage Ring (CESR) and the CLEO II detector. In Chapter 3, we present the detailed data analysis. Finally in Chapter 4, we compare our new result with various model calculations.

1.2 The Standard Model

High energy physics studies the elementary constituents that make up the physical world and the laws that govern their interactions. It's the modern scientific endeavor to answer the age-old question of "What is the world made of and how does it work?" at the most fundamental level.

After a half-century of vigorous theoretical and experimental exploration a clear picture has emerged, and it is captured in a theoretical framework collectively known as "The Standard Model".

The basic description of Standard Model on the fundamental structure of the physical world and the way it works can be summarized as "All matter is made of half-spin fermions—quarks and leptons, and they interact with each other in a unique symmetry pattern through the exchange of integer spin 'force carrier' bosons". The unique symmetry pattern is the $SU(3) \otimes SU(2) \otimes U(1)$ local gauge invariance group.

At the current experiment level, quarks and leptons don't appear to have any size or inner structures (above $10^{-18}m$), so they are now considered to be the most fundamental building blocks of the physical world.

Leptons and quarks exist in three generations, their properties are summarized in Table 1.1 [1].

Table 1.1: Three generations of leptons and quarks

Lepton	Charge	Mass(MeV)	Quark	Charge	Mass(MeV)
e	-1	0.511	d	-1/3	5-15
ν_e	0	$<$ 5.1 eV	u	2/3	2-8
μ	-1	105.7	s	-1/3	100-300
ν_μ	0	$<$ 0.17	c	2/3	1000-1600
τ	-1	1777	b	-1/3	4100-4500
ν_τ	0	$<$ 24	t	2/3	180,000

Three out of the four forces in nature, namely, the electro-magnetic, the weak and the strong force, are now unified under the Standard Model. Gravity, though the oldest fundamental force discovered by man-kind, is yet to be brought under the fold. Their characteristics are listed in Table 1.2

Table 1.2: Fundamental forces and their mediators

Force	Strong	Electro-magnetic	Weak	Gravity
Mediator	Gluon	Photon	$W^\pm, Z^0$	Graviton
number of quanta	8	1	3	1
Spin	1	1	1	2
Mass(GeV/c^2)	0	0	80.1,91.2	0
Range(m)	10^{-15}	∞	10^{-17}	∞
Relative Strength	1	$\alpha = 1/137$	10^{-5}	10^{-38}
Coupling Fermions	q	$l^\pm, q$	$(l^\pm \nu_l)$, (qq')	all with mass

Extensive experimental tests have been conducted against the Standard Model's predictions on elementary particle behaviors. So far the Model's predictions have stood very well. Still, the Standard Model can not be viewed as the "Final Theory" since there are many free parameters in the Model that still lack a deeper theoretical understanding of their origin and have to be determined experimentally and an array of questions remained unanswered. Among them are the origin of three generations of quarks and leptons, their unique mass pattern and the origin of quark weak mixing angles and whether quarks and leptons are really fundamental.

Currently, both theoretical and experimental efforts are made to push the envelope of high energy physics "beyond the Standard Model".

1.3 Electroweak Interactions and the The CKM Matrix

In the unified W-S electroweak theory, the electro-magnetic and weak forces are different manifestation of a single gauge field with $SU(2) \otimes U(1)$ local gauge symmetry. The symmetry is spontaneously broken by coupling with scalar Higgs doublet and gives rise to the large mass $W^{\pm}, Z^0$ as the weak force carriers, and the massless γ as the electro-magnetic force carrier.

After symmetry breaking, the charged weak current ($W^{\pm}$) part of the Lagrangian density can be expressed as

$$\mathcal{L}_{int} = -\frac{g}{\sqrt{2}}[J^{\mu}_{cc} W^{\dagger}_{\mu} + H.C.], \tag{1.1}$$

where

$$J^{\mu}_{cc} = (\bar{\nu}_e,\ \bar{\nu}_{\mu},\ \bar{\nu}_{\tau})\,\gamma^{\mu} \begin{pmatrix} e_L \\ \mu_L \\ \tau_L \end{pmatrix} + (\bar{u}_L,\ \bar{c}_L,\ \bar{t}_L)\,\gamma^{\mu} V \begin{pmatrix} d_L \\ s_L \\ b_L \end{pmatrix} \tag{1.2}$$

and V is the Cabibbo-Kobayashi-Maskawa (CKM) matrix:

$$V = \begin{pmatrix} V_{ud} & V_{us} & V_{ub} \\ V_{cd} & V_{cs} & V_{cb} \\ V_{td} & V_{ts} & V_{tb} \end{pmatrix}. \tag{1.3}$$

The CKM matrix V[2] relates the mass eigenstates to the weak eigenstates and is responsible for the direct quark coupling between different generations, which is absent in the lepton case. The existence of this quark weak mixing matrix generates a very rich pattern of hadronic interactions and is the focus of heavy flavor physics (b, c quarks) study.

By requiring the matrix to be unitary and by selecting the least number of complex phases through field redefinition, we can reduce the nine complex matrix elements to four independent real parameters. These parameters are fundamental constants of nature that need to be determined from experiment.

Through the Wolfenstein parameterization the matrix can be expressed in terms of powers of λ [3]

$$V = \begin{pmatrix} 1-\lambda^2/2 & \lambda & A\lambda^3(\rho - i\eta) \\ -\lambda & 1-\lambda^2/2 & A\lambda^2 \\ A\lambda^3(1-\rho-i\eta) & -A\lambda^2 & 1 \end{pmatrix} . \tag{1.4}$$

Here we only list to the order of λ^3. The Standard Model explains CP violation, such as observed in the K^o decays, in term of the λ^4 order effect in the V_{cs} value. λ, the sine value of the Cabibbo angle θ, and A have been determined from charged-current weak decays. The measured values are already relatively precise: $\lambda = 0.2205 \pm 0.0018$ and A=0.784±0.043. Here we are mostly interested in the determination of ρ and η.

The unitarity constraint of the CKM matrix yields six relationships $V_{ij}V^*_{ik} = \delta_{jk}$ and $V_{ij}V^*_{kj} = \delta_{ik}$, of which the most useful one is

$$V_{ud}V^*_{td} + V_{us}V^*_{ts} + V_{ub}V^*_{tb} = 0 \quad . \tag{1.5}$$

If we consider

$$V_{ud} \approx V^*_{tb} \approx 1 \;\text{ and }\; V^*_{ts} \approx -V_{cb} \;\; and \;\; V_{us} = \lambda. \tag{1.6}$$

then on the complex $\rho - \eta$ plane of CKM matrix values, this defines a triangle

$$\frac{V_{ub}}{V_{cb}} + \frac{V^*_{td}}{V_{cb}} - \lambda = 0 \quad . \tag{1.7}$$

with sides [4]

$$1 \tag{1.8}$$

$$\left|\frac{V_{td}}{A\lambda^3}\right| = \frac{1}{\lambda}\sqrt{(\rho-1)^2+\eta^2} = \frac{1}{\lambda}\left|\frac{V_{td}}{V_{ts}}\right| \tag{1.9}$$

$$\left|\frac{V_{ub}}{A\lambda^3}\right| = \frac{1}{\lambda}\sqrt{\rho^2+\eta^2} = \frac{1}{\lambda}\left|\frac{V_{ub}}{V_{cb}}\right|. \tag{1.10}$$

The CKM triangle is depicted in Fig. 1.1.

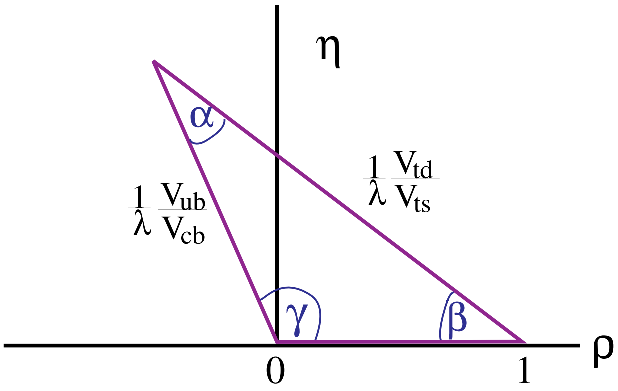

Figure 1.1: The unitarity triangle shown in the $\rho - \eta$ complex plane. The left side can be determined by measurements of $b \to u/b \to c$ processes and the right side can be determined using mixing measurements in the B_s and B_d systems. The angles can be determined through measuring CP violating asymmetries in exclusive hadronic B decays.

The angles α, β, and γ in Fig. 1.1, can be determined by measuring CP violation in rare hadronic B decays.

It is of great importance to see if measurements of heavy quark decays agree with the Unitary Triangle shown here, specifically whether the sides and angles can actually form a perfect triangle. This will be a critical test for the Standard Model and may shed the first light beyond the Standard Model.

The left side of the Unitarity Triangle can be determined through measurements of $|V_{ub}/V_{cb}|$, like the B semileptonic decay rates into c or u quark mesons. The right side can be determined using mixing measurements in the neutral B systems.

1.3.1 Neutral B Mixing and the determination of ρ, η

Neutral B mesons can transform to their anti-particles through the "Box Diagram" before they decay. The diagrams for B_d mixing are shown in Fig. 1.2. This process is dominated by the exchange of the t quark due to its huge mass.

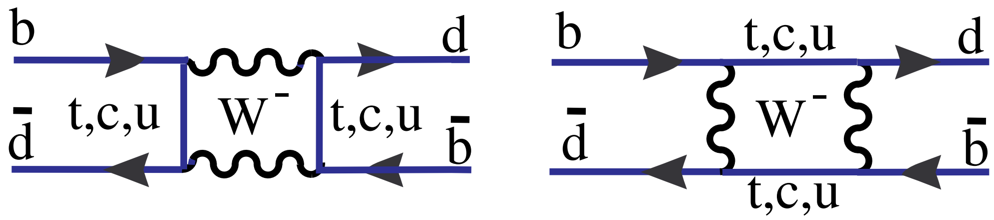

Figure 1.2: The two diagrams for B_d mixing.

The mixing rate is given by [5]

$$x \equiv \frac{\Delta m}{\Gamma} = \frac{G_F^2}{6\pi^2} B_B f_B^2 m_B \tau_B |V_{tb}^* V_{td}|^2 m_t^2 F\left(\frac{m_t^2}{M_W^2}\right) \eta_{QCD}, \tag{1.11}$$

where B_B is a parameter related to the probability of the d and $\bar{b}$ quarks forming a hadron and must be estimated theoretically; F is a known function which increases approximately as m_t^2, and η_{QCD} is a QCD correction, with value about 0.8. And f_B is the decay constant, which parameterizes the wave-function overlap of the two constituent quarks at zero spatial separation.

Since

$$|V_{tb}^* V_{td}|^2 \propto |(1 - \rho - i\eta)|^2 = (\rho - 1)^2 + \eta^2, \tag{1.12}$$

therefore neutral B mixing constraint will show as a circle centered at (1,0) in the $\rho - \eta$ plane.

The best mixing result so far come from LEP measurement, where time-dependent oscillations have been measured. Averaging over all LEP experiments x=0.728±0.025 [6].

Another constraint on ρ and η is from the K_L^o CP violation measurement (ϵ) [7]:

$$\eta\left[(1-\rho)A^2(1.4\pm 0.2)+0.35\right]A^2\frac{B_K}{0.75}=(0.30\pm 0.06), \tag{1.13}$$

where B_K is a parameter that cannot be measured and thus must be calculated. Here $0.9 > B_k > 0.6$ is used by an assortment of theoretical calculations [7]; this number is one of the largest sources of uncertainty. The other large uncertainty is in the CKM parameter A.

Fig. 1.3 shows the current status of constraints on ρ and η through the measurements mentioned above. The errors used are $\pm 1\sigma$ and they are all dominated by theoretical errors, most noticeably error on f_B calculation. This shows that the experimental data are consistent with the Standard Model description but we still can't derive the precise ρ and η values from these rate measurements because of the theoretical uncertainty in the parameters used.

1.4 Pseudoscalar-Meson Decay Constants

We can see by far the largest uncertainty in deriving ρ, η values arises from the decay constant, f_B. The decay constants describe the nonperturbative physics associated with quarks binding into mesons and are a source of great activity for theorists doing Lattice Gauge, QCD sum Rules, and Quark Model calculations.

The decay constant of f_P for pseudoscalar meson P is defined by [8]

$$< 0|A_\mu(0)V_{qq'}|P(\mathbf{q}) >= if_P q_\mu \tag{1.14}$$

where A_μ is the axial-vector part of the charged weak current. The state vector is normalized by $< P(\mathbf{q})|P(\mathbf{q}') >= (2\pi)^3 2E_q\delta(\mathbf{q}-\mathbf{q}')$, and its phase is chosen to make the f_P real and positive.

In principle the value could be determined directly from the leptonic B decay rate, either $B^+ \to \mu^+\nu$ or to $\tau^+\nu$. These purely leptonic decays are understood

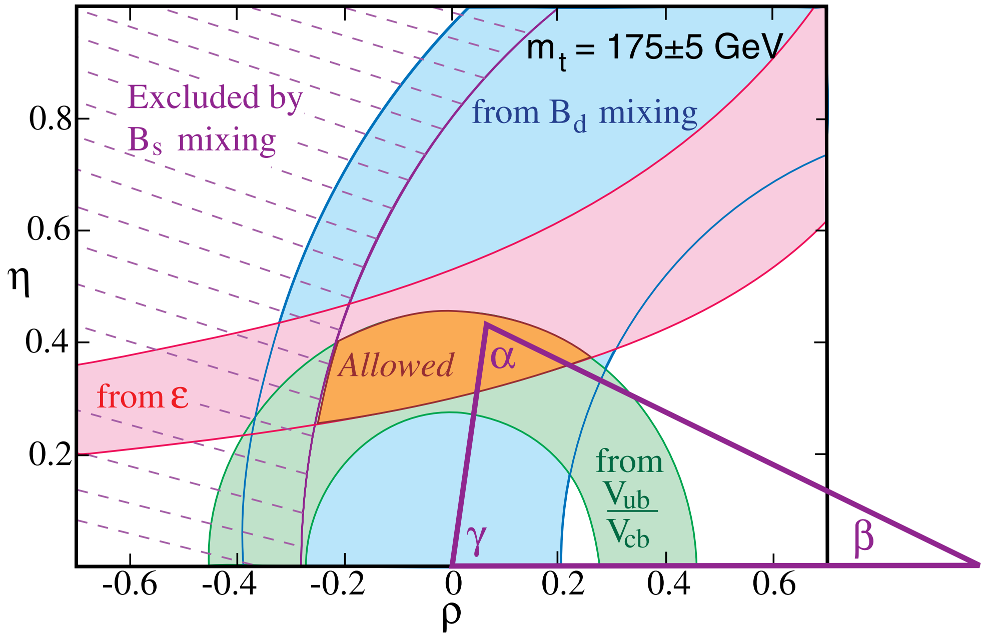

Figure 1.3: The regions in $\rho - \eta$ space (shaded) consistent with measurements of CP violation in K_L^o decay (ϵ), V_{ub}/V_{cb} in semileptonic B decay, B_d^o mixing, and the excluded region from limits on B_s^o mixing. The allowed region is defined by the overlap of the 3 permitted areas, and is where the apex of the CKM triangle sits. The bands represent $\pm 1\sigma$ errors. The large width of the B_d mixing band is dominated by the uncertainty in the parameter f_B. Here the range is taken as $240 > f_B > 160$ MeV.

theoretically to occur via an annihilation of the two quarks and the rate is directly sensitive to the meson decay constants. Fig. 1.4 depicts this process.

When determining f_P experimentally, radiative corrections must be taken into account, since the photon-loop correction introduces an infrared divergence that is canceled by soft-photon emission. For B decays there is an additional component in that the radiative rate may be enhanced by other effect [9].

Currently, it is not possible to determine f_B experimentally from leptonic B decays. The latest L3 [10], CLEO [11] and other results [12] show that the upper limits on these modes are still at least one order of magnitude higher than the Standard Model prediction. So theoretical QCD calculations of f_B must be used to extract ρ, η.

Measurements of the Cabibbo-favored pseudoscalar decay constants such as f_{D_s}

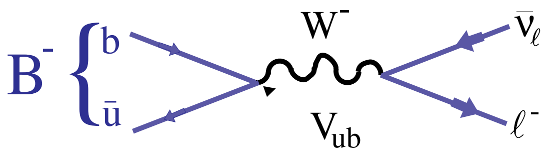

Figure 1.4: The diagram for B^- annihilation into two letopns.

provide a check on these calculations and help discriminate among different models and calibrate these calculations.

1.5 Measurement of f_{D_s}

The decay rate for D_s^+ is given by [13] [14]

$$\Gamma(D_s^+ \to l^+\nu) = \frac{G_F^2}{8\pi} f_{D_s}^2 m_l^2 M_{D_s} \left(1 - \frac{m_l^2}{M_{D_s}^2}\right)^2 |V_{cs}|^2 \quad , \tag{1.15}$$

where M_{D_s} is the D_s mass, m_l is the mass of the final state lepton, V_{cs} is a CKM matrix element equal to 0.974 [15], and G_F is the Fermi coupling constant. Various theoretical predictions of f_{D_s} range from 190 MeV to 350 MeV. Note there is a helicity suppression term m_l^2 in the equation. This is a because of the two body nature of the decay. The back-to-back leptons must make a spin-0 final state, but the neutrino is left handed and forces the positively charged lepton to this helicity, which introduces a factor of the lepton mass in the amplitude. In the end the decay rate is suppressed by the factor $(m_l/m_P)^2$, m_P is the heavy meson mass. Because of helicity suppression, the electron mode $D_s^+ \to e^+\nu$ has a very small rate and is practically inaccessible compared with the tau and muon modes. The relative widths are $10 : 1 : (2 \times 10^{-5})$ for the $\tau^+\nu$, $\mu^+\nu$ and $e^+\nu$ final states, respectively. Unfortunately the mode with the largest branching fraction, $\tau^+\nu$, has at least two neutrinos in the final state and is difficult to detect.

In a previous publication [16], CLEO reported the measurement of $f_{D_s} = (344 \pm 37 \pm 52 \pm 42)$ MeV, using the decay sequence $D_s^{*+} \to \gamma D_s^+$, $D_s^+ \to \mu^+\nu$. Three other groups have also published the observation of $D_s^+ \to \mu^+\nu$ and extracted values of f_{D_s}. WA75 reported f_{D_s} as $(232 \pm 45 \pm 20 \pm 48)$ MeV using muons from D_s^+ leptonic decays seen in emulsions [17]; BES measured a value of $(430^{+150}_{-130} \pm 40)$ MeV by fully reconstructing D_s^+ mesons close to the production threshold in e^+e^- collisions [18]; and E653 extracted a value of $(194 \pm 35 \pm 20 \pm 14)$ MeV from one prong decays into muons seen in an emulsion target [19].

In this document we present an improved CLEO analysis. We use a sample of about 5 million $e^+e^- \to c\bar{c}$ events collected with the CLEO II detector [20] at CESR. The integrated luminosity is 4.79 fb^{-1} at the $\Upsilon(4S)$ resonance or at energies just below. This new result supersedes our previous result which was based on a subset of the current data with 2.13 fb^{-1}. The improvements include a better analysis algorithm, more data, more precise measurements of the lepton fakes, and reduced systematic uncertainties.

Chapter 2

CESR and the CLEO II Experiment

The data used in this analysis were collected with the CLEO II detector at the Cornell Electron Storage Ring (CESR) from 27 May, 1990 to 9 April, 1995. The Datasets used include 4s-1 to 4s-G. The integrated luminosity is 4.79 fb^{-1} at the $\Upsilon(4S)$ resonance or at energies just below. This corresponds to about 5 million $e^+e^- \to c\bar{c}$ events

2.1 The Cornell Electron Storage Ring (CESR)

The Cornell Electron Storage Ring (CESR) is an electron-positron collider machine which covers the center of mass energy range between 9 and 12 GeV. It is located 50 feet underground on Cornell campus with a circumference of about half-mile. It was constructed in 1977-1979 and started operation in 1979. CESR has excellent peak luminosity and now holds the world record for integrated luminosity collected by a colliding beam accelerator. It regularly runs at 10.58 GeV, which is the $\Upsilon(4S)$ region, or at energy level just below.

Figure 2.1 shows a schematic configuration of the CESR accelerator/storage ring complex. CESR is composed of four major components: LINAC–the linear accelerator, the circular synchrotron, the storage ring and interaction region. The building at the south end that houses CLEO, CHESS detectors and LINAC is called Wilson Laboratory, where physicists take shifts to control the operation of CESR and CLEO all year around.

The linear accelerator (LINAC) is the source that produces the electrons and positrons and initially accelerates these particles. The electrons are emitted from a headed filament and accelerated by a cathode and then compressed into a small bunch. This bunch is then accelerated along a 100-foot vacuum pipe by a series of radio-frequency (RF) cavities. Electrons reach an energy of 300 MeV at the end of LINAC and are injected into the synchrotron counter-clockwise.

Positrons are produced by colliding the accelerated electrons at an intermediate point with a tungsten target. The target generates electron and positron showers. The positrons are picked up by a magnet and accelerated to 150 MeV and then guided into the synchrotron clockwise.

The circular synchrotron is the primary accelerator that accelerates the electrons and positrons to the energy of interest. It consists of a vacuum beam pipe and 192 10-foot long sections of bending magnets and four 10-foot long 500 MHz RF cavities used to accelerate electrons or positrons in the same beam pipe. Positrons are accelerated and injected into the storage ring first until they reach a desired current. The electrons are filled next.

Because the electrons and positrons travel in a curve, they radiate photons. This by-product is called synchrotron radiation. The radiation is used by CHESS as intense X-ray source to study solid-state material micro-structures and biological molecular samples, like proteins.

Prior to March 1994, both electron and positron beams were composed of seven evenly spaced bunches colliding head-on at the interaction point. To avoid unwanted collisions at the other 13 intersections, electrostatic separators with a potential difference of 25,000 volts were used to separate the two beams.

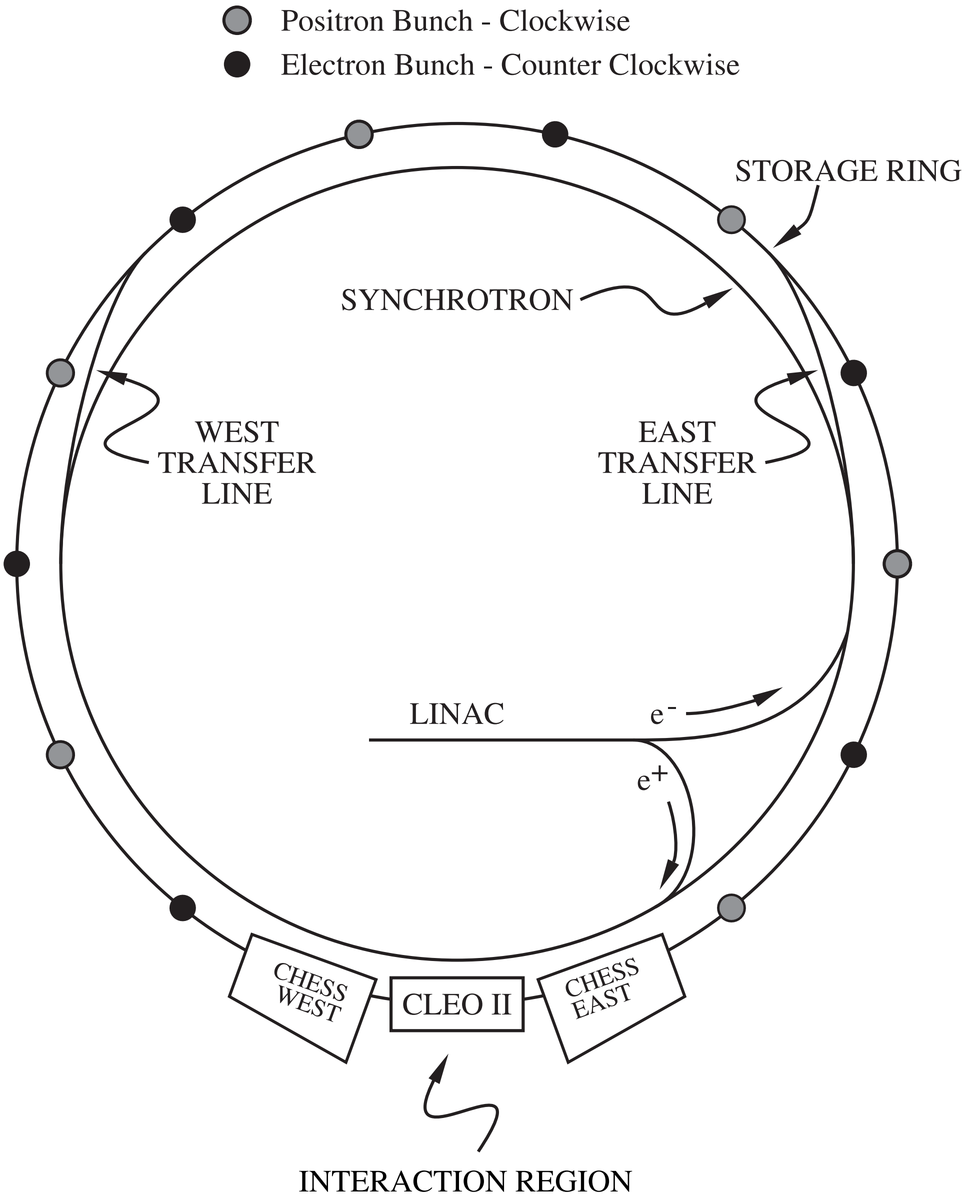

Figure 2.1: The Cornell Electron Storage Ring.

Since then the CESR beam configuration has been changed to be composed of 9 trains, each consisting of several closely spaced bunches that cross each other at a small horizontal crossing angle. This increases the peak luminosity by a large margin. The small crossing angle is needed to reduce unwanted collisions between the closely spaced tiny bunches at places very close to the interaction point.

Typically after about one hour of colliding, a considerable amount of beam has been lost in the storage ring and it therefore becomes more efficient to halt collisions and refill the machine. Usually the positron beam is kept and replenished while the electron beam is dumped to be totally refilled.

At the interaction region, which is positioned to be at the exact center of the CLEO II detector, the electrons and positrons bunches collide each other to generate interesting physics events. The size of the intersection region is about 18 mm wide along the beam, 500 μm in the horizontal and 10 μm in the vertical direction.

2.2 CLEO II Detector

The CLEO II detector [21] is a large multi-component, general purpose high energy physics detector designed to achieve excellent detection resolution and efficiency for both charged and neutral particles. It contains over 900 tons of iron and over 25,000 detection elements and about 6 meters in each dimension. All its detector elements have cylindrical symmetry and are concentric with the beam pipe.

Fig 2.2 and Fig 2.3 show the the side-view of the different components making up the CLEO II detector. The main components are the beam pipe, the tracking chambers(PTL, VD, DC), the time of flight (TF) particle ID, the crystal calorimeter (CC) for electromagnetic shower detection, the superconducting magnet and the muon chambers (MU). Because of the moderate momentum range, no hadronic calorimeter is used.

Different kinds of information from all the detector components are used in this analysis.

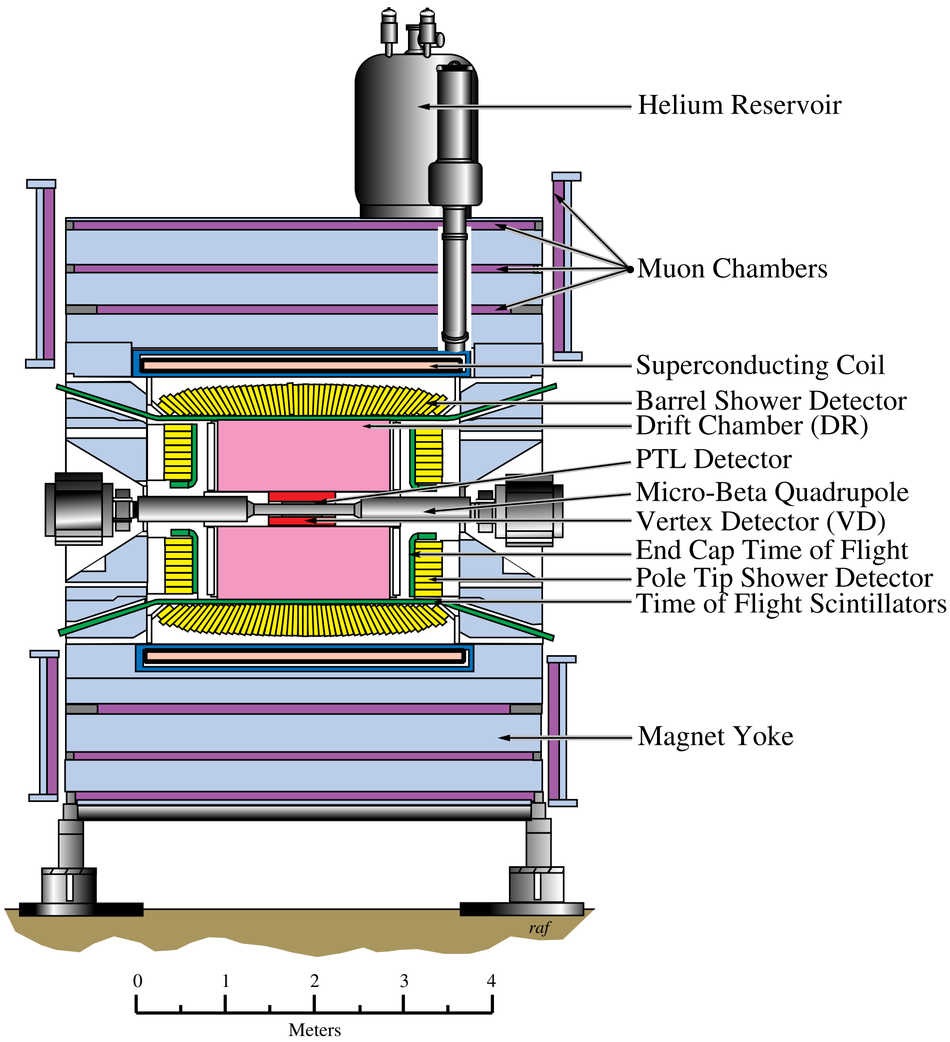

Figure 2.2: Side view of the CLEO II detector.

2.2.1 Beam Pipe

The beam pipe surrounding the interaction point is a thin-walled low radiation length (0.44%) beryllium (Be) pipe with 3.5 cm radius and a wall thickness of mere 0.5 mm. It is coated with a 25 μm silver and 1 μm nickel films to reduce background from

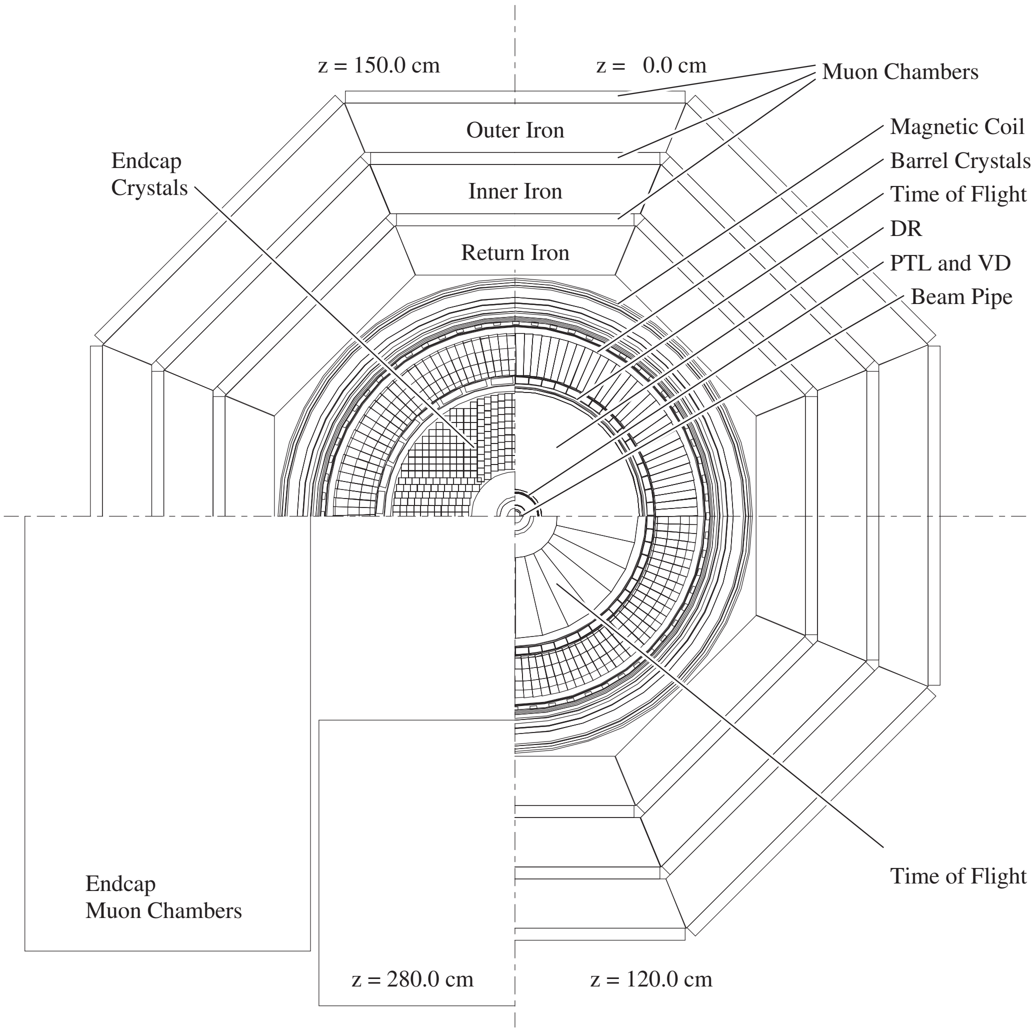

Figure 2.3: Cross-section view of the CLEO II detector. Each quadrant of the detector has been "sliced" at a different distance along the beam axis to show the end-cap structure.

synchrotron radiation in the detector. The beam pipe design allows the inner tracking layers to be close to the interaction point, while minimizing the material between the interaction point and the detector. The pipe is 33 cm long and subtends a solid angle 99% of 4π.

2.2.2 Tracking Chambers

The three innermost detector components (PTL, VD and DR), collectively called Central Detector, are all drift chambers with different design that measure the ionization of gas as a charged particle passes through in order to determine the momentum vector and identity of the particle. This arrangement aims to achieve different goals with separate chambers that would be difficult to simultaneously meet with a single design.

PTL

The main purpose of the precision tracking layers (PTL) detector is to detect the primary vertex in $r-\phi$ with precision. It contains 384 polycarbonate tubes in 6 layers, 64 tubes each layer. Each tube is 45 cm long and has an axial anode sense wire of 15 μm gold plated tungsten with tension of 22 grams. The cathodes are the aluminized tubes. The resolution achieved is 100 microns in the $r-\phi$ plane. The PTL does not provide longitudinal measurement of charged tracks because it is so close to the interaction point. PTL runs with a gas mixture about 50% argon and 50% ethane at 1 atm.

With CLEO II.5 upgrade about two years ago, the PTL was replaced with a 3 layer silicon vertex detector with double sided silicon strip elements, that increased the $r-\phi$ spatial resolution to 10 micron level. Data from these runs are not included in this analysis.

VD

The vertex detector (VD) is 90 cm long with an active length of 72 cm and radius from 8.1 cm to 16.6 cm. It contains 800 sense wires and 2272 field wires that are arranged in 10 layers to form small hexagonal cells. The inner 5 layers have 64 cells, and the outer 5 layers, 96 cells each. The structure is shown in Fig.2.4 The gas used is the same mixture as for the PTL but with a small amount of C_2H_5OH added to reduce organic compounds building up on the wires from high voltage discharge. The VD is operated at 20 psi (about 1.38 atm, can go up to 2 atm) pressure to provide for more ionization for the small cell size and to be insensitive to atmospheric pressure variations. Signals are read out on both ends of the VD wires to obtain the axial coordinate through charge division.

DR

The outer drift chamber (DR) is the main tracking volume for the CLEO II detector, together with PTL and VD, it provides measurements of charged particle momentum vectors and ionization energy loss (dE/dx) for particle identification. The cell structure, shown in Fig. 2.5 is 14 mm by 14 mm each. The inner radius is 17.5 cm, and the outer radius is 95 cm. There are total of 12,240 sense wires and 36,240 field wires arranged in 51 layers. Out of the 51 layers, 40 are axial layers and they are separated by 11 stereo layers. The stereo layers have sense wires strung at a slant angle relative to the axial direction to give longitudinal information. The slant angle of these layers alternates in sign and increases from 1.91^0 to 3.50^0 as radius increases. The layers are arranged in 10 "superlayers" with 3 axial layers and one stereo layers up to layer 40 and then 2 "superlayers" of 5 axial layers and one stereo layer. The length of the wires is 192.4 cm. The sense wires are 20 μm diameter gold plated tungsten strung with tension of 50 grams. The field wires of layer 1 to layer 40 are 100 μm gold plated 5056-aluminum with tension of 170 grams. The field wires of layer 41 to layer 51 are

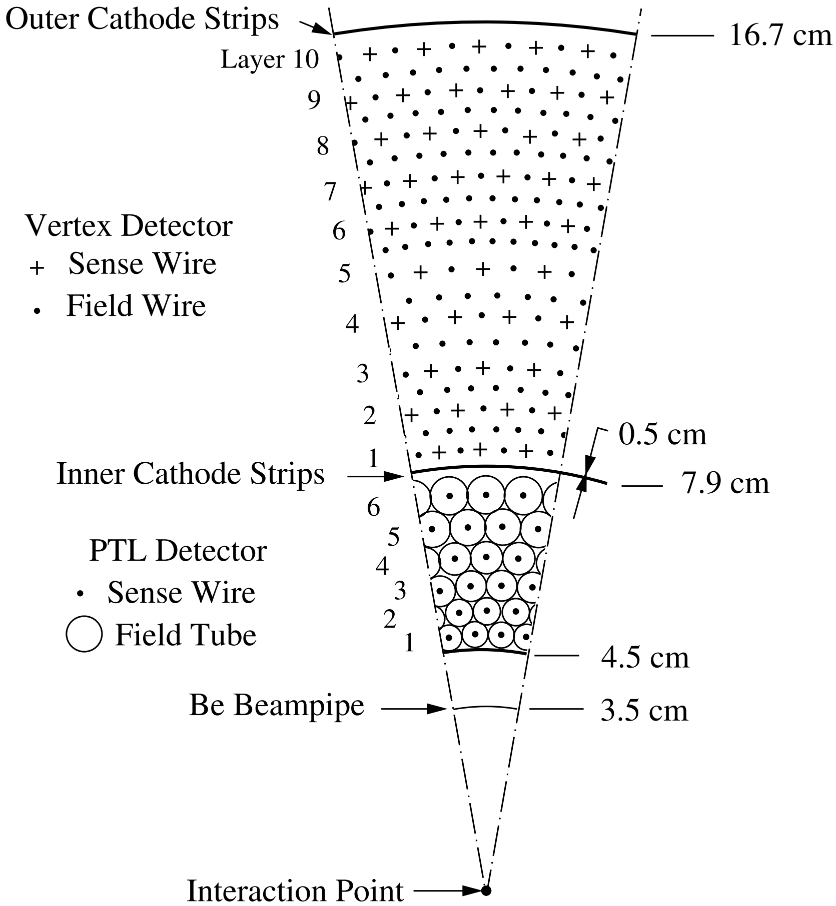

Figure 2.4: Cell structure of VD and PTL.

110 μm gold plated copper-beryllium strung with a tension of 270 grams. The total tension from these strung wires put huge stress on the aluminum endplates so they have to be thick, 1.25 inch, to provide the mechanical strength. The sense wires are put under positive voltage, typically 2050V, and the field wires are kept at ground. The gas mixture used is the same as PTL.

With 1.5 Tesla magnetic field, momentum resolution can be parameterized as: [22],

$$\left(\frac{\delta p}{p}\right)^2 = (0.005)^2 + (0.0015)^2 p^2 \tag{2.1}$$

where the momentum, p, is measured in GeV. The first term is due to individual measurement errors in the drift distances; the second one is due to track distortion from multiple Coulomb scattering in the detector material.

Study of the $e^+e^- \to \mu^+\mu^-$ sample shows that the resolution of azimuthal and polar angles is

$$\delta\phi = 1\ mrad; \quad \delta\theta = 4\ mrad \tag{2.2}$$

These values include the multiple scattering effect but are valid only for this process. Resolution found in hadron events are slightly worse.

2.2.3 Time of Flight

The Time-of-Flight (TOF) system serves two purposes. First it is used as a primary trigger for data acquisition because of its fast response time. Secondly it is used as a tool for particle identification for low momentum tracks. It determines the particle species by measuring the difference between the time of the beam crossing and when a particle strikes a scintillator and calculate the velocity. Using momentum measurements from tracking chambers, the mass of a particle can be determined.

The barrel ToF consists of 64 plastic scintillation counters mounted just outside the central drift chamber, with a light guide and photo multiplier at each end. Figure

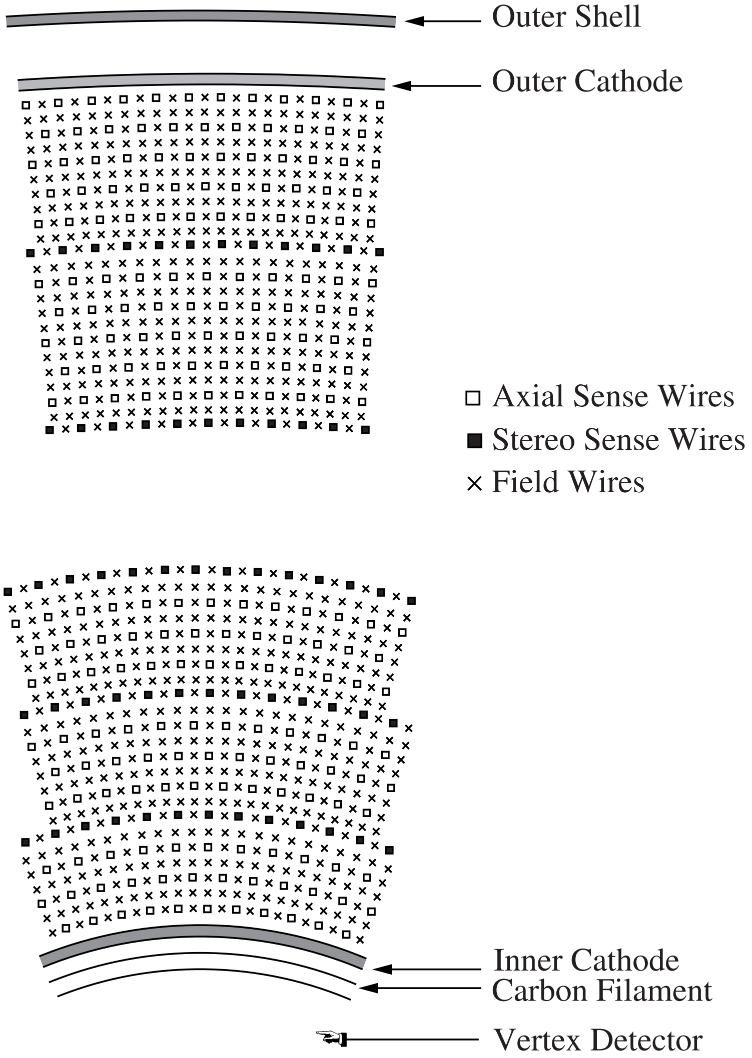

Figure 2.5: Cell structure of drift chamber.

2.6 shows the geometry of a single counter.

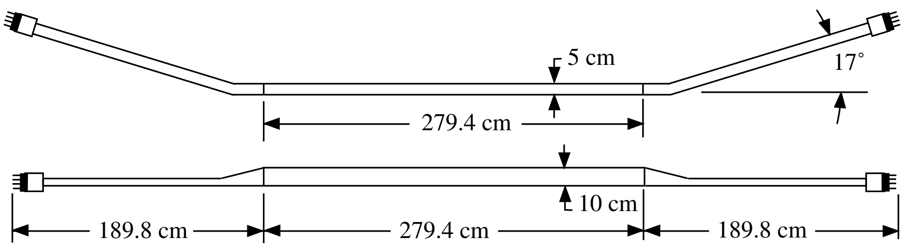

Figure 2.6: Barrel TOF sintillators.

2.2.4 Charged Particle Identification

When analyzing CLEO II data, TOF and dE/dx information is often used together for particle identification, mostly to distinguish the kaons from the pions. Figure 2.7 shows a scatter plot of $1/\beta$ derived from the ToF versus the momentum. Figure 2.8 shows the $K^{\pm}$ and $\pi^{\pm}$ separation using the dE/dx information. We can see the separation in the 1 to 2 GeV momentum range is no better than a 2σ.

The particle ID information is critical for CP violation measurements like $B^0 \to K^-\pi^+$ and $B^0 \to \pi^-\pi^+$. Both decays generate energetic (about 2.5 GeV/c) kaons and pions that currently are barely distinguishable with CLEO II particle ID

So one major objective of the CLEO III upgrade is to achieve excellent $K-\pi$ separation up to 2.8 GeV/c. The particle identification detector chosen for CLEO III is a Ring Imaging CHerenkov (RICH) detector which is being developed and constructed by the High Energy Physics group at Syracuse in collaboration with other CLEO groups. It is designed to provide excellent (4 σ) $K-\pi$ separation for track momentum up to 2.5 GeV/c. The author of this thesis was involved in the design, testing and construction effort of CLEO III RICH.

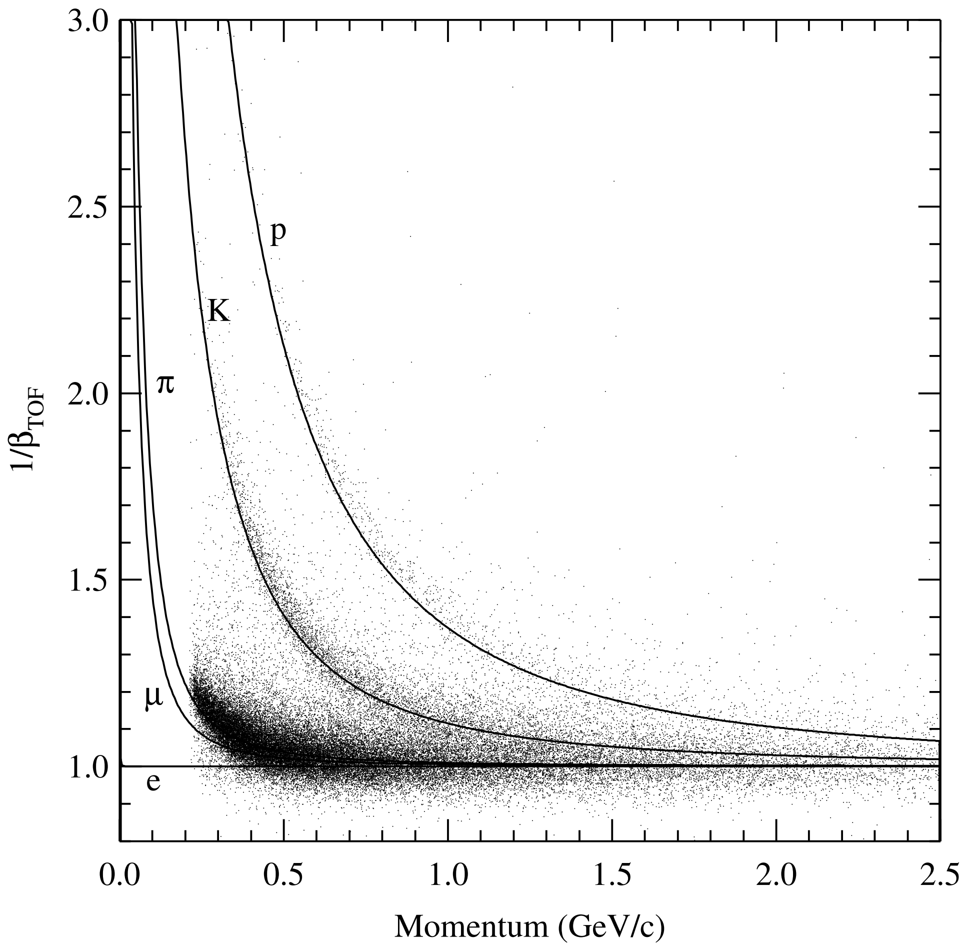

Figure 2.7: Time of Flight $1/\beta$ measurement versus particle momentum. The mean of the different particle hypothesis are shown.

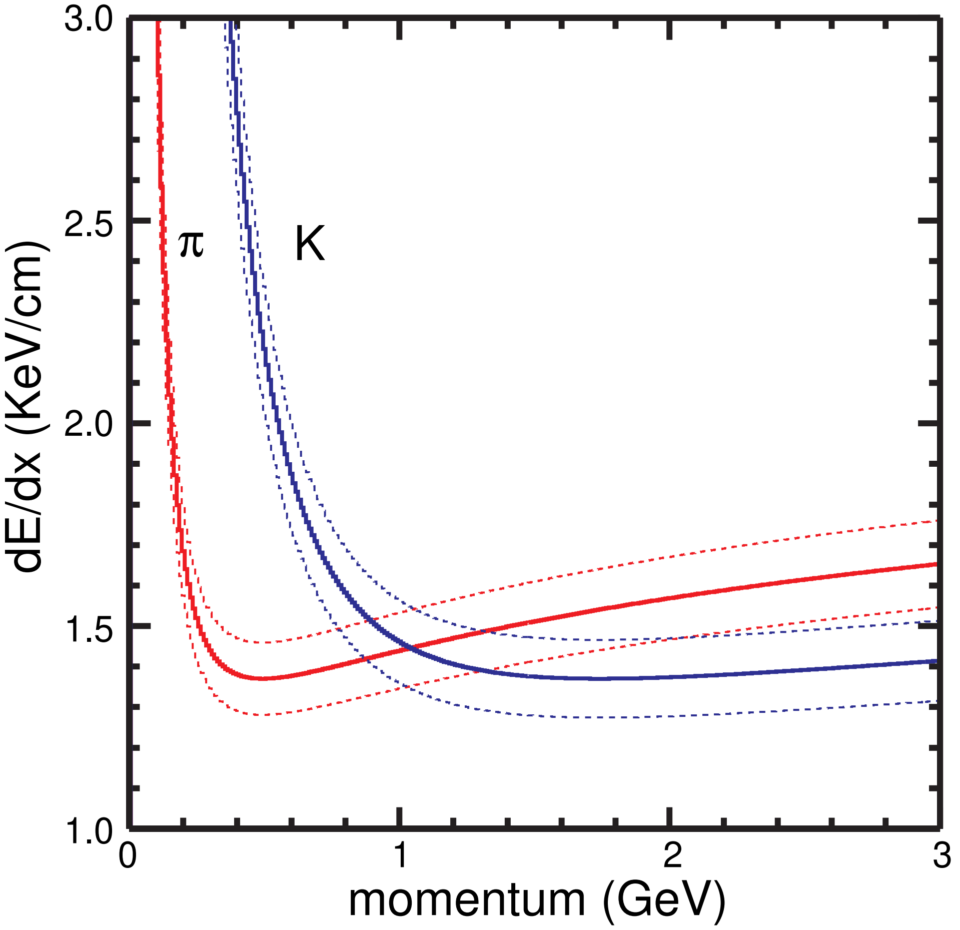

Figure 2.8: $K - \pi$ separation using specific ionization information. The solid line denotes the mean while the dashed lines are the 1σ boundaries.

2.2.5 Crystal Calorimeter

The CLEO II crystal calorimeter is a fine-grained, large volume electromagnetic shower detector system. It is composed of 7800 thallium doped cesium iodide (CsI) crystals grouped into one barrel and two endcap regions which all together cover 95% of the solid angle. Each crystal is about 5×5 cm^2 in cross-section and 30 cm long. There are 6144 crystals laid in a radial fashion towards the interaction point in the barrel. And 828 rectangular crystals are laid horizontally in each endcap, divided into 4 sections. An electron or photon hitting a dense crystal produces an electro-magnetic shower. The energy of the shower causes scintillation in the crystal and the light intensity is proportional to the shower energy. The scintillation light is collected by 4 square shaped photo-diodes placed at the end of the each crystal. Each diode has a its own preamplifier and the signals from 4 diodes of one crystal feed through separate cables into the mixer/shaper card locates outside the CLEO II detector. There the four signals from one crystal are summed and shaped for input to the ADC. Four diodes are used for reason of failure redundancy. If a substantial gain ratio change is detected, the problem preamplifier will be shut off and the gain will be automaticly readjusted.

A light flasher system monitors changes in the calibration of the photodiodes and an electronic pulser calibration monitors the readout electronics down-stream of the diodes for pedestal and gain ratio drifts. Crystal to crystal calibration is conducted by collecting data sample of Bhabha events, which contains beam energy electron-positron pairs.

With these sophisticated calibrations the CLEO II calorimeter performs superbly. The resolution is given by [21]

$$Barrel: \quad \frac{\sigma_E}{E}(\%) = \frac{0.35}{E^{0.75}} + 1.9 - 0.1E \tag{2.3}$$

$$Endcap: \quad \frac{\sigma_E}{E}(\%) = \frac{0.26}{E^{0.75}} + 2.5 \tag{2.4}$$

The angular resolution is given by

$$Barrel: \quad \sigma_\phi(mrad) = \frac{2.8}{\sqrt{E}} + 1.9, \quad \sigma_\theta(mrad) = 0.8\sigma_\phi sin(\theta) \tag{2.5}$$

$$Endcap: \quad \sigma_\phi(mrad) = \frac{3.7}{\sqrt{E}} + 7.3, \quad \sigma_{theta}(mrad) = \frac{1.4\sigma}{\sqrt{E}} + 5.6 \tag{2.6}$$

where the photon energy E is measured in GeV. For a 2.5 GeV photon, the energy resolution is $\sigma_E(2.5\ \text{GeV}) = 46$ MeV.

The low energy resolution is limited mostly by the electronic noise. The resolution for high energy photons is dominated by rear-end energy leakage [21]. In the intermediate energy range, the scintillation yield fluctuation dominates the resolution.

The Crystal Calorimeter also plays the critical role of electron identification. Both electrons and photons in the momentum range studied are totally stopped by CC. An electron shower is different from a photon shower by having a charged track pointing to the center of the shower cluster. And the measured track momentum (P) should agree with the detected shower energy E. That is E/P should be very close to 1. Most other hadron tracks $(K, \pi, P...)$ leave a small amount of energy deposit in CC and pass through. So the E/P ratios are much smaller than 1. Even when they do hit a nucleon and react, the "split-off" particle products often travel far across inside CC and have a different (unsymmetric) lateral shape than an electro-magnetic shower. This can be discriminated by cutting on the shape variable ($E9/E25$) which is the ratio of the energy deposit in the 3×3 crystals over in the 5×5 crystals, with the largest output crystal at the center. Occasionally, however, a hadron track will pass all these electron signature cuts and be misidentified as an electron. For high momentum tracks, there is no other particle ID information available, then they become hadronic lepton fakes. Though CLEO II does a very good job in suppressing this hadronic lepton fake rate, the small rate still has a very significant role in this analysis.

2.2.6 Super-conducting Magnet

The drift chambers, ToF, and crystal calorimeter are placed within a 1.5 Tesla super-conducting magnet. The magnet is 3.5 m long, 3.1 m in diameter, and covers 95% of the solid angle in the drift chamber volume. The uniform magnetic field is parallel to the beam axis and is used to bend the charged particles in the $r - \phi$ plane. The curvature of a charged particle's trajectory within the magnetic field is used to determine the particle's momentum.

2.2.7 Muon Chambers

Unlike electrons, muons can penetrate through large distances of solid matter before being finally absorbed. So in a typical high energy detector complex, the muon detector is staged in the outermost space. The muon identification system for CLEO II was designed with the goals of maximum solid angle coverage, high efficiency, low hadron fake rate, reliability and ease of operation. Syracuse High Energy Group designed and constructed the muon system.

Because of space limitations the muon chambers only cover the polar angle range 30° to 150°, which is 85% of the total solid angle.

The barrel portion of the muon detector consists of eight octants that are symmetrically positioned parallel to the beam axis. Endcap units cover the two ends of the detector. Barrel muon chambers are sandwiched between three layers of iron absorber, which stop other kinds of particles. The iron plates are also used for the magnetic return yoke. The three layers are labeled as "Return", "Inner", and "Outer", respectively. The endcaps have only one layer of tracking. The total equivalent thickness of the iron absorbers varies from 7.2 to 10 nuclear absorption lengths, depending on the direction of the track.

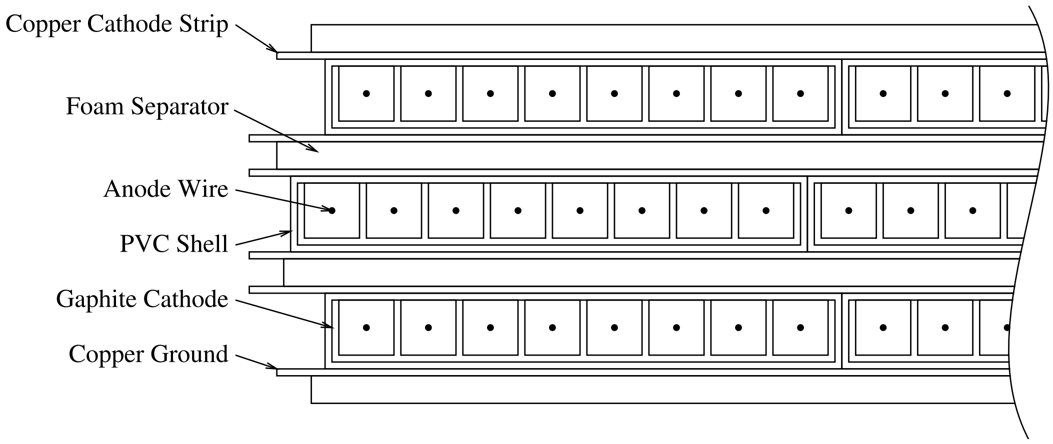

Figure 2.9: Cross section of one muon chamber superlayer

The chambers are plastic streamer counters, operating in the proportional mode, at 2500V with the standard CLEO gas mixture. The counters are about 5 meters long and 8.3 cm wide each (see Fig 2.9). The plastic tubes are graphite coated on three sides to provide the cathode and each tube has a 50 μm gold plated tungsten anode wire which provides the one coordinate of the hits. The orthogonal coordinate is provided by copper stripes that run perpendicular to the tubes on the side which is not coated with graphite. The spatial resolution is 2.4 cm for counters and 2.8 cm to 5.5 cm for the strips.

The set of all counters in a steel gap is called a unit. each unit consists of three staggered layers of 20, 25, 29, or 24 counters for the return, inner, outer or endcap units respectively. Each layer of counters is divided into two multiplets of 10 to 15 counters while the copper strips are divided into four multiplets of either 9 or 15 strips each. Members of the multiplets are connected to their neighbors via 100 Ω resistors. To save the number of electronic channels needed for readout, charge division is used to determine which counter or strip was hit.

Muon identification is carried out by extrapolating into the muon detector each track reconstructed in the tracking chambers, taking into account ionization energy loss. The path length in each muon layer is calculated in terms of nuclear absorption length. Then a search is made for hits in the muon units that are likely to be traversed by the track and a two-dimensional χ^2 of the distance between the measured and the projected hit positions is calculated. If the χ^2 is less than 16, that layer is considered to be hit. The track is considered as definitely detected in a superlayer if at least two out of the three layers are hit.

The track is assigned the depth of the outermost unit in which it is detected. If there are other units at greater depth that, according to track extrapolation, are expected to be hit but there are no hits in those units, then the track is considered as a non-muon. Also, a track is considered a bad quality muon candidate if it fails to give at least one associated layer hit in each of the units along its path at a depth less than the maximal one.

Since there is no hadronic calorimeter to stop the charged hadron tracks, they can reach the muon chamber and a small number of the very energetic ones can penetrate through all the three layers of iron absorbers. This will cause the hadron to be misidentified as a muon. And generally the muon fake rate is larger than the electron fake rate. Since these muon-faking hadrons constitute a substantial background for this analysis, the fake rate of energetic hadrons is precisely measured in this analysis.

2.3 Trigger and Data Acquisition

With the current beam configuration, beam crossing time is about 140 ns or 7 MHz in terms of crossing frequency and events of various kinds can happen at each beam crossing. The production rate of beauty and charm quark events and other physics events of interest, including some events for calibration purposes, however is around ten events per second. Given the huge number of channels and detector response time, sophisticated trigger mechanism is needed to filter away unwanted events and record only those events of interest. This is accomplished by a combination of hardware and online software that swiftly recognizes certain event characteristics to make trigger decision.

Currently the trigger rate achieved is around 30Hz with a detector live time ratio over 90%. The maximum trigger rate is therefore dead-time limited.

The CLEO II trigger system is tiered with three levels. Level 0 (L0) makes fast, simple decisions that can keep pace with the beam crossing rate. It uses inputs from the TOF, VD, and CC to reduce the 2.7 MHz crossing frequency to a rate about 20 kHz. L0 trigger controls whether to disable the electronic gates used to collect detector response information like pulse heights.

Level 1 (L1) trigger uses inputs from the TOF, VD, DR, and CC. Preparation time for these devices to be ready for L1 is approximately 1.0 μs, so a L0 rate of 20 kHz gives at least of 2% dead time. L1 is needed to reduce from the L0 rate to 25 Hz so that online data collection rate from all the detector channels can match data storage (disk) rate. If no L1 criteria have been met, the trigger logic is reset and gating of the experiment resumes.

Each set of L1 criteria has a specific set of Level 2 (L2) criteria. At present only VD and DR contribute to L2. The readiness time of L2 in now 50 μs. Since L1 rate does not exceed 50 Hz, this wait for L2 results in only 0.25% dead-time. As with L1, if no proper L2 criteria are met the system is reset and gating resumes.

A software level trigger Level 3 (L3) are used to reject the unwanted events and reduce the amount of data for off-line processes. The L3 trigger runs online but causes no dead-time since it only filters data and does not deal with raw data taking process.

The detector electronics is arranged in crates containing ADC's for digitization and memory for storing pedestals and other constants. Once the trigger system has decided that an event of interest has occurred, the data from the CLEO II detector must be read out by the data acquisition (DAQ90) system [23]. Fig 2.10 shows a schematic of the DAQ90 system.

2.3.1 $\Upsilon(4S)$

Figure 2.11 shows the hadronic cross-section for $e^+e^- \to q\bar{q}$ as a function of center of mass energy. The first three resonance peaks in the cross-section correspond to production of bound $b\bar{b}$ states. The fourth radial excitation of this system $\Upsilon(4S)$ is just above kinematic threshold for the production of B mesons ($B = b\bar{q}$, where $q = u, d$). At $\Upsilon(4S)$, about one fourth of the hadronic events are $e^+e^- \to b\bar{b}$ and the rest are continuum events of $e^+e^- \to u\bar{u}$, $d\bar{d}$, $s\bar{s}$ and $c\bar{c}$. The continuum cross-section is approximately 3.26 nb [24, 25].

2.4 Data Processing

Data taken from the data acquisition system are first analyzed on-line, using simplified reconstruction called PASS1 to quickly reconstruct charged tracks and neutral bumps of a selected number of the events. The goal is mainly for on-line diagnostic rather than physics analysis. Histograms based on this reconstruction are inspected at the end of each run in order to catch any detector or collider problem as quickly as possible. All events are written to tape for off-line processing. Based on the different physics process type, events are categorized into dimuons, Bhabhas and radiative Bhabhas or hadronic events, etc. Calibration constants are generated from a subset of data called skim to register the detector characteristics for that run.

After all calibration constants have been produced, the main off-line reconstruction program called PASS2 is run. This program finds tracks in the tracking chambers,

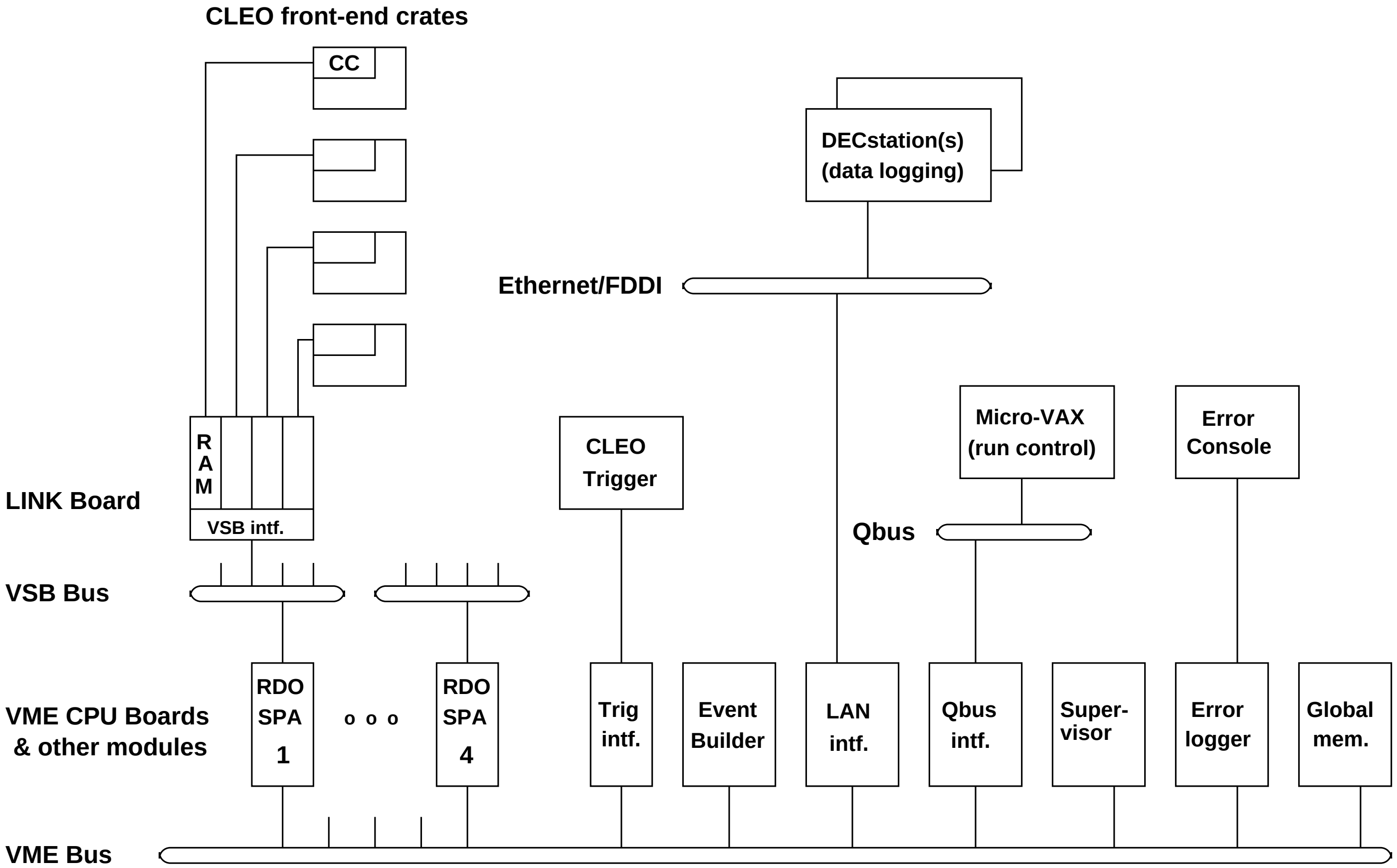

Figure 2.10: The CLEO II DAQ90 data acquisition system.

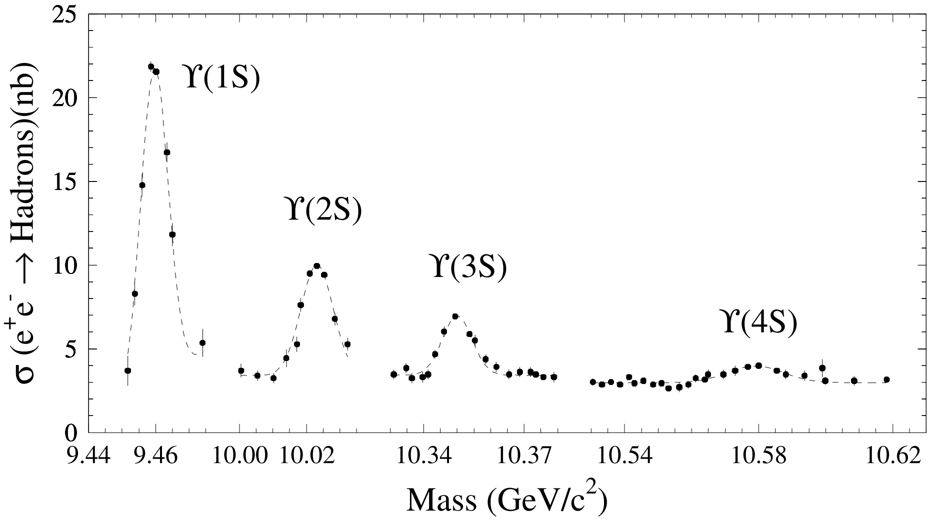

Figure 2.11: Cross-section for $e^+e^- \to$ hadrons.

clusters in the calorimeter performs other general utility tasks. The output of this program, written in uncompressed format, contains all the raw information from the detector, as well as all of the processed information added in the off-line reconstruction. A typical hadronic event contains 40 K-Bytes of data. We then store the events in a compressed format that only retains the analyzed information. This reduces the typical size to 1.5 K-Bytes. All the analysis was perform using these compressed data format.

2.5 Monte Carlo Event Simulation

In order to understand the decay kinematics of the physics events under study and the complex detector response, Monte Carlo simulations of the whole process are generated and they produce data in the same format as the real raw data. Monte Carlo events are then analyzed to study the signal and background shapes and levels and to determine the optimal selection criteria on event variables for best signal to background ratio and reconstructing efficiency. This is usually the starting point of physics data analysis.

The Monte Carlo events are generated in two steps. The first step is to generate desired decay process using an event generator called QQ. The purpose is to study the kinematics of the chain of physics events. A file that contains a linear table of particle properties, including mass, charge, spin, decay modes, decay branching ratios, helicity, etc., is the major input. This defines all the "generic" decay modes. To study particular decay processes, the user often override certain default entry to generate just the process of interest. A control file is also needed to define the class of basic interaction, like $e^+e^- \to \Upsilon(4S)$ or $\to B\bar{B}$, or $\to$ non-resonant $q\bar{q}$ production,etc., Given these inputs, QQ will iterate through the decay table and generate a set of final-state particles through the interaction process defined in the control file.

The second step of Monte Carlo simulation is to simulate the propagation of the decay products of QQ through the CLEO II detector using a GEANT [27] based program called CLEOG. CLEOG simulates the particle–detector interaction in CLEO II and the corresponding detector response of all the electronic readout channels. CLEOG contains a full geometric description of the CLEO II detector, the materials and the response of the detector elements, and a interface with QQ. It takes particles from QQ and tracks them through the detector as they travel outward under the influence of the magnetic filed, recording their trajectories and those of any daughters. Some decay-in-fly particles are produced by CLEOG internally. The output files' format is identical to that of the raw data from real detector. CLEOG output also contains the QQ information which define the decay process and kinematics, allowing determination of efficiencies, losses and mismeasurements of the detector. Finally these simulated raw data are processed with PASS2 just like real data.

Chapter 3

Measurement of $\Gamma(D_s^+ \to \mu^+\nu)/\Gamma(D_s^+ \to \phi\pi^+)$ and f_{Ds}

3.1 Analysis Method Overview

Since the CLEO II detector has excellent detection resolution for both charged and neutral particles, in order to improve signal identification, we search for the decay chain $D_s^{*+} \to \gamma D_s^+$, $D_s^+ \to \mu^+\nu$. This is because D_s^{*+} dominantly decay into $D_s^+\gamma$ and about half of the energetic D_s^+ come from D_s^{*+}. (See 3.4.7)

The photon from the D_s^{*+} decay and the muon from the $D_s^+ \to \mu^+\nu$ decay are measured directly, while the neutrino is measured indirectly by using the near-hermeticity of the CLEO II detector to determine missing momentum and energy. Using the missing momentum as the neutrino momentum, we look for a signal in the mass difference

$$\Delta M = M(\gamma\mu^+\nu) - M(\mu^+\nu), \tag{3.1}$$

so that the relatively large errors from the missing momentum calculation will mostly cancel.

Charm fragmentation is known to produce energetic particles so we require the D_s^{*+} candidates to have momenta above 2.4 GeV/c.

To study the ΔM signal and background shapes and to evaluate the effectiveness of our Monte Carlo simulation for detection efficiency , we also collect a data sample of similar topology, $D^{*o} \to \gamma D^o$, $D^o \to K^-\pi^+$. We treat these fully reconstructed data events as $D_s^+ \to \mu^+\nu$ decays by removing the measurements of the π^+ from both the tracking chambers and the calorimeter to simulate the ν, and by using the K^- as if it were a muon. Our aim here is to compare the Monte Carlo simulation of these D^{*o} decays with what we obtain from the data.

Another useful event sample consists of the decay sequence $D^{*+} \to \pi^+ D^o$, $D^o \to K^-\pi^+$, since this sample has relatively high statistics and negligible background. We use these events to study the missing energy and momentum measurements by eliminating the measurements of the fast π^+ from the D^o decay from both the tracking chambers and calorimeter to simulate the neutrino, and call the K^- a muon.

3.2 Background

3.2.1 Physics background

There are several potential sources of background in this measurement. The most important one is the real lepton background. There are many charm decays that can generate an energetic muon and a soft photon in the process, such as charm semileptonic decays. These real physics backgrounds are almost identical in muon and electron final states because of lepton universality. For the leptonic D_s^+ decay, however, the electronic width is negligible in comparison to the muonic width due to the helicity suppression. Thus, performing the identical analysis except for selecting electrons rather than muons gives us a quantitative measurement of the background level due to real leptons. This is one of the important techniques in this analysis and it requires having a very accurate measurement of all background levels involved and a good handle on the signal shape parameters since we can not rely on the $D_s^+ \to \mu^+\nu$

data to give us this information. This requirement drives most of the analysis effort.

$D_s^+ \to \mu^+\nu$ and $D^+ \to \mu^+\nu$ decays are the only physics processes that produce significantly more primary muons than electrons with momenta above 2 GeV/c in continuum e^+e^- annihilations in the $\Upsilon(4S)$ energy region. The $D^+ \to \mu^+\nu$ decay background in our sample is highly suppressed by the CKM angle (Eq. 1.15), and by the small $D^{*+} \to \gamma D^+$ branching ratio, $(1.4 \pm 0.5 \pm 0.6)\%$ [28].

3.2.2 Hadron/Lepton fake background

Another source of background results from the misidentification of hadrons as muons (fakes). Since muon identification in CLEO II has larger fake rates than electron identification, we need to consider the excess fakes in the muon sample relative to the electron sample. To determine the hadron-induced muon and electron fake background contributions, we multiply the ΔM distribution of all tracks, excluding identified leptons, by an effective hadron-to-lepton fake rate, measured with tagged hadronic track samples. The detailed analysis of this effective fake rate is described in Section 3.5.

3.2.3 Random photon background

After removing the above two components, all remaining events result from either $D_s^{*+} \to \gamma D_s^+$, $D_s^+ \to \mu\nu$ decays, or from spurious combinations of random photons and real $D_s^+ \to \mu^+\nu$ and $D^+ \to \mu^+\nu$ decays. The shape of the latter component is determined using the fully reconstructed $D^{*+} \to \pi^+ D^o, D^o \to K^-\pi^+$ data sample, and the normalization is determining by measuring the D_s^{*+}/D_s^+ production ratio. Subsequently, we will form a single signal shape from these two signal components.

3.3 Event Selection and Background Suppression

3.3.1 Event selection

Most of the leptons from B meson decays are removed by requiring a minimum lepton momentum of 2.4 GeV/c, which is 33% efficient for $D_s^+ \to \mu^+\nu$. Leptons from $\tau^+\tau^-$ pairs, and other QED processes with low multiplicity, are suppressed by requiring that the event either has at least five well reconstructed charged tracks, or at least three charged tracks accompanied by at least six neutral energy clusters. To suppress background from particles that escape detection at large cos θ, where θ is the angle with respect to the beam axis, we require that the angle between the missing momentum of the event and the beam axis, θ_{miss}, does not point along the beam direction, specifically $|\cos\,\theta_{miss}| < 0.9$.

3.3.2 Lepton identification and efficiencies

Muons are required to penetrate at least seven interaction lengths of iron, and to have $|\cos\,\theta| < 0.85$. The muon identification efficiency, measured with $e^+e^- \to \mu^+\mu^-\gamma$ events, is (85±1)% for muons above 2.4 GeV and is very flat in momentum. Electrons must have an energy deposit in the electromagnetic calorimeter close to the fitted track momentum, and a dE/dx measurement in the main drift chamber consistent with that expected for electrons. The electron identification efficiency for $|\cos\,\theta| < 0.85$, is found by embedding tracks from radiative Bhabha events into hadronic events. For electrons with momentum greater than 2.4 GeV, a value of (89±2)% is used.

3.3.3 Relative muon/electron ratio normalization

To subtract the electron data from the muon data we need to have a precise measure of the muon to electron normalization. Detector material causes a difference between muons and electrons, as electrons tend to radiate more. The correction factor is estimated to lower the electron rate by 5%: thus we assign a +5% increase in the electron sample due to this outer bremsstrahlung. A Monte Carlo study shows that the main background contributions from real leptons in the ΔM distribution are semileptonic D decays, mostly $D \to K\ell\nu$, $\pi\ell\nu$ and $\eta l\nu$. As a specific example of the near equality of the muon and electron rates we made a detailed study of the $D^+ \to K^o\ell^+\nu$ decay. A calculation of the different probabilities that a photon is emitted in the decay (inner bremsstrahlung) for $D^+ \to K^o l^+\nu$ was performed according to the prescription of Atwood and Marciano [29]. This effect raises the electron rate by +2.7%. This inner bremsstrahlung correction for the different semileptonic final states averages also to +2.7%. We also correct for differences in muon and electron phase space, which lowers the relative electron normalization (−1.7% for $D^+ \to K^o l^+\nu$). Taking all of these sources into account, including the different possible decay modes and the fact that the electron detection efficiency is 4% larger than the muon efficiency, we use a correction factor of 1.01±0.03 to multiply the electron sample to account for the physics backgrounds and the identification efficiency difference.

3.3.4 Photon selection

Photons must be in the angular region $|\cos\theta| < 0.71$. We require a minimum energy of 150 MeV, which is 78% efficient for $D_s^{*+} \to \gamma D_s^+$ decay, to eliminate backgrounds caused by the large number of low energy photons. Combinations of two photons which have invariant masses within two standard deviations of the π^o mass are eliminated. (The r.m.s. π^o mass resolution is 5 MeV.) We also insist that in the rest frame of the D_s^{*+} candidate, the cosine of the angle between the photon and the D_s^{*+} direction in the lab be larger than −0.7. A small residual $b \to ul\nu$ background is suppressed by requiring that the thrust axis lines up with the D_s^{*+} candidate momentum so that the cosine of the angle between them is greater than 0.975.

3.4 Signal Shape and Efficiency

3.4.1 Neutrino reconstruction

To evaluate the neutrino four-vector we measure the missing momentum and energy in only half of the event; we divide the event into two hemispheres using the thrust axis of the event. The missing momentum $\vec{p}_{miss}$ and energy E_{miss} are calculated using only energy and momentum measurements $(E_i, \vec{p}_i)$ in the hemisphere that contains the lepton (kaon). We compute the energy sum assuming all tracks are pions, unless they are positively identified as kaons, or protons by dE/dx measurement in the drift chamber. We define the missing momentum and energy as

$$\begin{aligned} \vec{p}_{miss} &= \vec{p}_{thrust} - \sum \vec{p}_i \quad \text{and} \\ E_{miss} &= E_{beam} - \sum E_i \quad , \end{aligned} \tag{3.2}$$

where the direction of $\vec{p}_{thrust}$ is given by the thrust axis. The magnitude is $p^2_{thrust} = E^2_{beam} - m^2_{jet}$, where E_{beam} is the beam energy and m_{jet} is the average mass of a charm quark jet, measured to be 3.2 GeV using our sample of fully reconstructed D^{*+} events [30]. A D_s^+ candidate is selected by requiring 1.2 GeV $< M(\mu^+\nu) <$ 3.0 GeV, and that the missing mass squared be consistent with a neutrino, $|E^2_{miss} - p^2_{miss}| < 2$ GeV^2, where the cut values are based on studies using the D^{*+} events. Furthermore, we also require $p_{miss} > 0.8$ GeV/c to suppress backgrounds, since real $D_s^+ \to \mu^+\nu$ events must have some missing momentum. The D_s^{*+} candidate momentum is required to be above 2.4 GeV/c. We find a factor of two increase in efficiency by using only one hemisphere to determine the missing momentum relative to using the whole event.

3.4.2 D_s mass constrained neutrino momentum error correction

To improve the signal resolution and efficiency, we looked for new constraint to incorporate in the final ΔM determination.

In this analysis, there are two decay processes. $D_s^{*+} \to D_s^+\gamma$, and the subsequent $D_s^+ \to \mu^+\nu$. The kinematic constraint of the D_s^{*+} decay is already used to calculate ΔM. For the D_s^+ decay, however, we only make a cut on the reconstructed D_s^+ mass; the decay constraint itself is not used in determining the ΔM signal. Because of the poor resolution of neutrino reconstruction, the D_s^+ mass distribution is therefore very wide, (We made a 2σ cut of 1.6 GeV to 2.6 GeV). By using D_s^{*+}-D_s^+ mass difference as the signal, much of this error cancels out, but the remaining width (18 Mev low side, 27 Mev high side) of the ΔM signal shape due to this neutrino resolution is still significantly larger than in the fully reconstructed D_s^{*+}-D_s^+ mass difference as in the $D_s^+ \to \phi\pi^+$ channel (about 5 MeV, mostly from γ resolution)

For our first attempt we tried to employ a standard mass constrained fitting program to do a D_s^+ mass constrained $\mu\nu$ reconstruction. It turned out that determining the covariant error matrix for our neutrino candidate is difficult. One way to do this is to use Monte Carlo simulation to determine the errors on neutrino reconstruction. However Monte Carlo is not a reliable way to determine these errors. Another way is to sum up all the errors of the tracks and neutral bumps used in reconstructing the neutrino, but if there is a K_L or neutron in the event, then this approach is wrong. Still another way is to use the D^{*0} data sample discussed in previous text, since we have the information of the "rejected" pion in addition to the reconstructed neutrino, we can compare them directly and get the error for neutrino measurement. However K_L is still a problem here since D^{*0} jets fragment differently from D_s^{*+} jets. We tried all these approaches but did not get any significant resolution improvement, and in some cases the resolution gets worse.

After some further study of the decay kinematics, we figured that there is a more straightforward and physically more meaningful way to incorporate the D_s^+ decay constraint. Note that, compared to the neutrino, the muon should be considered very "accurately" measured, much of the error comes from the neutrino measurement. So we can focus on how to "adjust" the reconstructed neutrino position relative to the muon to make the "correct" D_s^+ mass.

The following are the decay equations for the $D_s^+ \to \mu^+\nu$ process,

$$E_{D_s} = E_\mu + E_\nu \quad \text{and} \tag{3.3}$$

$$\overrightarrow{p}_{D_s} = \overrightarrow{p}_\mu + \overrightarrow{p}_\nu \tag{3.4}$$

In the local coordinate frame defined by the selected muon, by assuming the neutrino mass to be zero, we get,

$$\sqrt{m^2_{D_s^+} + p^2_{D_s^+}} = \sqrt{m_\mu^2 + p_\mu^2} + p_\nu \quad \text{and} \tag{3.5}$$

$$p^2_{D_s^+} = p_\mu^2 + p_\nu^2 + 2p_\mu p_\nu cos\theta \tag{3.6}$$

where θ is the opening angle between the selected muon and any "right" neutrino 3-vector.

Squaring Eq. 3.5 and plugging it into Eq. 3.6 and rearranging shows a relationship between p_ν and the cosine of the angle between the muon and neutrino:

$$p_\nu = \left(m_\mu^2 + m_{D_s}^2\right) / \left(2p_\mu \cos\theta - 2E_\mu\right), \quad \text{where } \mathrm{E}_\mu = \sqrt{\mathrm{m}_\mu^2 + \mathrm{p}_\mu^2}. \tag{3.7}$$

which describes the shape of a ellipsoid in 3-D space around the muon momentum vector, as shown in Fig. 3.2.

By assuming the parent particle to be a D_s^+, we thus incorporate the D_s^+ decay constraint into the process: any neutrino candidate which satisfies the D_s^+ decay constraint must sit on this ellipsoid.

Since we already have a reconstructed neutrino candidate, and often it's likely away from the D_s^+ mass ellipsoid surface, (actually, the distance corresponds to its D_s^+ mass resolution) one natural way of determining a best adjusted neutrino position on the surface would be to require that the distance between the adjusted neutrino on the ellipsoid and the reconstructed neutrino candidate to be minimum. Globally, this would define a single point on the ellipsoid, which lay on the same plane of the muon and the reconstructed neutrino.

Instead of solving the minimization equations and finding the analytical solution, which would be very tedious, we developed a numerical solution algorithm by iterating through only the section of the ellipsoid which is physically meaningful in our analysis (e.g. up to 5.3 GeV) and recursively searching for the regional global minimum. By carefully choosing the iteration boundary and steps, our algorithm converges pretty rapidly. Once we found this optimized neutrino position, we convert its coordinates from the muon local frame to the lab frame and use it to do the D_s^{*+} reconstruction and derive the ΔM value.

Using Monte Carlo, we see that the ΔM signal using the new "fitted" neutrino momentum with D_s^+ mass constraint is significantly higher and narrower than using just the reconstructed neutrino position directly (as shown in Fig. 3.1, it's about 40% higher and 30% narrower).

A more careful look at the geometry shows that the improvement comes mostly from correcting the error of the reconstructed neutrino that diverges away from the D_s^+ ellipsoid surface. The "real" neutrino must lay somewhere on the surface, and our neutrino reconstruction resolution could be considered isotropic, thus one standard deviation surface will be a sphere around the "real" neutrino position. Any error along the ellipsoid surface is not corrected because of the lack of any further constraint. The interesting point is that the reconstructed neutrino that is farthest from the ellipsoid surface is best adjusted by getting the most accurate "adjusted" neutrino position. Because of this effect we decided to open up our M_{D_s} cut to increase efficiency.

One concern we had about this new technique was that we may distort the background shape and the background will condense towards the signal region too when we are shrinking the signal width. From the electron data shape in Fig. 3.11 (a) we can see this is not happening. This is largely due to the fact that though we adjusted the reconstructed neutrino momentum so that $(\mu\nu)$ mass has the D_s mass value, the soft gamma momentum is independent of this process. So there is no particular reason for random background to favor specific D_s^*/D_s mass difference value.

The advantage of this technique is that it is purely based on kinematics and geometric consideration; no specific knowledge of detection error is used except that one particle has much larger error than the other. So this technique can be used anywhere when we want to do mass constrained fitting and one daughter particle has large measurement error and the nature of the error is hard to determine (like in the neutrino case). The technique is not limited to two-body decays. In three-body decays like B meson semileptonic decays, we can combine the reconstructed charm meson and the charged lepton together and treat them as one particle to apply the same method here.

3.4.3 Signal shape parameters and checking using D^{*0} data samples

We use Monte Carlo simulation to determine the ΔM signal shape (Eq. 3.1) and to estimate our efficiency. Since this analysis involves reconstructing a missing neutrino, we are concerned that the Monte Carlo will not adequately simulate the data. As a check we evaluate the accuracy of our simulation using our $D^{*o} \to \gamma D^o$, $D^o \to K^-\pi^+$ sample, where we eliminate the π^+ to simulate the neutrino and treat the K^- as a muon.

We start with a $D^{*o} \to \gamma D^o$, $D^o \to K^-\pi^+$ Monte Carlo simulation. Fig. 3.3(a) shows the fully reconstructed mass difference $\Delta M = M(\gamma K\pi) - M(K\pi)$ distribution after a cut on the $K^-\pi^+$ invariant mass of ± 30 MeV around the known D^o mass (where the r.m.s resolution is 8 MeV). The kaon is required to have momentum greater than 2.4 GeV/c, which is the same cut as we use on the muon in the

$D_s^+ \to \mu^+\nu$ channel. In the ΔM distribution there is a substantial signal but also significant background, so a ΔM sideband subtraction is performed. We use a bin-by-bin subtraction. The central value of the signal is 142 MeV and the r.m.s. width is 5.5 MeV. The sidebands used are 114-126 MeV and 159-170 MeV. After applying the additional background suppression cuts, described above, we obtain the mass difference distribution $\Delta M = M(\gamma K p_{miss}) - M(K p_{miss})$ shown in Fig. 3.4. There is a clear signal peak associated with the photon and it is fitted to an asymmetric Gaussian with low side and high side σ's of 15 MeV and 16 MeV, respectively. The small flat component results from replacing the correct photon with another photon.

3.4.4 Neutrino detection efficiency

The partial efficiency for neutrino detection only from Monte Carlo for a fully reconstructed D^{*o} event with both the D^{*o} and its kaon daughter having a momentum greater than 2.4 GeV to appear in the signal peak after neutrino reconstruction is found to be ϵ_ν = (38.9±2.6)% [31]. The overall detection efficiency for $D^{*o} \to D^o\gamma$, $D^o \to K^+ p_{miss}$ is $(4.8 \pm 0.3)\%$ [32].

Next, we repeated the analysis described above for the fully reconstructed $D^{*o} \to \gamma D^o$ data sample. The fully reconstructed ΔM distribution is shown in Fig. 3.3(b). The ΔM distribution for the missing neutrino is shown in Fig. 3.5 where the sideband subtraction again has been performed. The fitting parameters derived from the Monte Carlo signal shape fit the data very well, with a χ^2 of 23 for 27 degrees of freedom and a confidence level of 69%. The partial efficiency for neutrino detection of (38.5±3.7)% agrees well with Monte Carlo simulation.

3.4.5 Total reconstruction efficiency

In principle the resolution and efficiency for $D_s^{*+} \to \gamma D_s^+$, $D_s^+ \to \mu^+\nu$ can be somewhat different from that for the D^{*o} sample described above, because of the different fragmentation with an s quark rather than a u quark. Since our Monte Carlo simulation accurately describes the $D^{*o} \to \gamma D^o$, $D^o \to K^-\pi^+$ process, we rely on it for our D_s^* study. In Fig. 3.6 we show the $\Delta M = M(\gamma\mu^+\nu) - M(\mu^+\nu)$ distribution from Monte Carlo simulation. This distribution contains a Gaussian part due to the signal, plus a flat part which occurs when the correct photon from the D_s^* decay is replaced with another random photon in the event. We fit the histogram with an asymmetric Gaussian signal shape having low side and high side σ's of 15 MeV and 17 MeV, and the function $\sqrt{x-x_0}e^{-a(x-x_0)}$ to parameterize the random photon component, where $x \equiv \Delta M$. The Gaussian signal shape agrees well with the D^{*o} Monte Carlo and data. Using the Gaussian signal part only, the overall efficiency is found to be $(4.2\pm0.3)\%$, where the error includes the systematic effect of the efficiency difference between data and Monte Carlo determined by the D^{*o} sample.

3.4.6 Residual random photon contribution

An additional source of events in the ΔM distribution comes from direct $D_s^+ \to \mu^+\nu$ decays that pair with a random photon to form a D_s^{*+} candidate. These are in addition to D_s^{*+} events where the correct photon is replaced by another photon, as mentioned above. These two signal contributions are fixed relative to the direct $D_s^{*+} \to \gamma D_s^+, D_s^+ \to \mu\nu$ signal using our measurement of the D_s^{*+}/D_s^+ production ratio above 2.4 GeV of 1.08 ± 0.13 (see below). Thirdly, there is a small contribution from $D^+ \to \mu^+\nu$ decays combined with a random photon. The shape in ΔM of all these contributions is modeled using the $D^{*+} \to \pi^+ D^o$ event sample, by combining the $M(Kp_{miss})$ candidates with random photons in the same event, and fitting with the functional form $\sqrt{x-x_0}e^{-a(x-x_0)}$ to parameterize the total random photon component. The distributions in Fig. 3.6 and the random photon component function are summed using appropriate weights to produce the expected shape for the sum of the $D_s^{*+} \to \gamma D_s^+,\ D_s^+ \to \mu^+\nu$ signal plus random photon background shown in Fig. 3.7.

3.4.7 Measurement of the D_s^+ and D_s^{*+} Rates

In order to measure the relative rates of D_s^* and D_s production, and the absolute level of D_s production above 2.4 GeV/c we use the $D_s^+ \to \phi\pi^+$ decay mode. The ϕ is searched for in the K^+K^- decay mode. We require the photon from the D_s^{*+} decay to satisfy the same requirements as for the $\mu^+\nu$ final state. The detection efficiency for the $\phi\pi^+$ decay mode is 22.3%, while for the D_s^{*+} the efficiency is 9.4% [33].

Fig. 3.8(a) shows both the invariant mass of the $\phi\pi^+$. In (b), we show $\Delta M = M(\gamma\phi\pi^+) - M(\phi\pi^+)$ after requiring that the $\phi\pi^+$ mass be within ± 24 MeV of the D_s^+ mass.

Fitting the data to Gaussian signals shapes whose widths are determined by Monte Carlo simulation we find 5728$\pm$123 $D_s^+ \to \phi\pi^+$ events and 1256$\pm$54 D_s^{*+} events. Taking into account the relative efficiencies we determine that the ratio of D_s^{*+}/D_s^+ production is 1.08$\pm$0.13. This number reflects the direct production of a vector charmed-strange meson relative to the direct production of a pseudoscalar charmed-strange meson, above 2.4 GeV/c [34].

3.5 Lepton Fake Background Calculation

Even after strict lepton identification requirements have been applied, significant numbers of fake leptons still enter our signal region because of the abundance of fast hadron tracks. To properly account for this hadron-faking-lepton background, we need to measure precisely the effective excess muon to electron fake rate ratio to derive the correct background level. The D^* decays provide us with well-tagged kaon and pion samples. In our previous publication, the uncertainty in the fake rate value dominated the systematic errors. One major improvement of the current analysis is the better determination of these rates for muons and electrons from much larger tagged data samples obtained by using new data and adding more channels.

In this analysis, in addition to the decay sequence $D^{*+} \to D^o\pi^+ \to (K^-\pi^+)\pi^+$, we also include $D^{*+} \to D^o\pi^+ \to (K^-\rho^+)\pi^+$, and $D^{*o} \to D^o\pi^o \to (K^-\pi^+)\pi^o$ to get as many events as possible. $K_S \to \pi^+\pi^-$ samples are also used to determine the pion fake rate and are combined with the D^* results to get better statistics. About 14,000 events were collected with either a π or K with momentum greater than 2.4 GeV from the above channels.

In Fig. 3.9 we show the $M(\pi^+K^-\pi^+) - M(K^-\pi^+)$ mass difference after a cut on $K\pi$ mass consistent with the D^o mass for kaons or pions which pass our cuts for muons or electrons The number of events is determined by a fit with a double Gaussian for the signal and half-integer power polynomials for background. Both fitting function shapes are derived from the mass difference distribution without lepton identification suppression. Our extracted fake rates (before decay in flight correction) are listed in Table 3.1. The same reconstruction methods are used to collect kaon and pion samples from the channels $D^o \to K^-\rho^+$, and $D^{*o} \to D^o\pi^o$ (where D^o goes to $K^-\pi^+$) samples. The fake rates are determined by fitting the mass distributions for the amount of signal. The fake rates derived from the different channels are summarized in Table 3.1, and the weighted average fake rates are also shown.

Table 3.1: Fake Rates for P > 2.4 GeV/c

Data Samples	# of K	# of π	Fake Rates (%)			
			K/μ	K/e	π/μ	π/e
$D^{*+}(D^o \to K^-\pi^+)$	9404	7461	0.94±0.11	0.04±0.05	0.60±0.12	0.24±0.06
$D^{*+}(D^o \to K^-\rho^+)$	1368	682	1.23±0.33	0.22±0.20	0.30±0.40	0.15±0.21
$D^{*o}(D^o \to K^-\pi^+)$	3174	2048	1.07±0.21	0.17±0.10	0.84±0.35	0.60±0.31
$K_S \to \pi^+\pi^-$	-	3527	-	-	0.74±0.15	0.37±0.10
Total/Average	13964	13718	0.98±0.08	0.12±0.05	0.65±0.08	0.31±0.06

3.5.1 Decay in flight contribution for fake rates

The contributions to the lepton fake rates from kaon and pion decays in flight are not necessarily included in the above procedure because particles decaying close to the production point may not appear in the D^o mass peak. To account for this effect, we used a Monte Carlo study of 200,000 $D^{*+} \to D^o\pi^+ \to (K^-\pi^+)\pi^+$ events. After muon identification cuts are applied, the D^{*+} mass difference plot has a peak region used to derive the fake signal and a tail away from the peak, which is due to events in which the kaon decays. We extract a correction factor to the fake rate of 1.18±0.06 by computing the ratio of the tail area to the peak area. We find no events out of the D^* mass difference peak in which the pion has decayed. This is because of the relatively long pion lifetime and because the muon momentum is very close to that of the parent pion.

We determine the hadron induced muon and electron fake background contributions by multiplying the ΔM distribution of all tracks, excluding leptons, by the effective fakes rates determined above. The fractions of kaon, pions and protons are 60%, 27% and 13% as ascertained from Monte Carlo simulation. The effective fake rates from protons and anti-protons are small, ≈0.1%, and almost equal for muons and electrons.

3.5.2 Momentum dependence of the fakes and fake rates

In Fig. 3.10 we show the momentum distribution of kaon and pion track candidates from Monte Carlo which pass all of our cuts and would enter into the ΔM signal region if they were identified as muons. Fig. 3.10 also shows the momentum distribution of muons coming from the $D_s^+ \to \mu^+\nu$ which should be the same as the kaon and pion distribution coming from the D^{*+} samples that we used for fake rate determination. The momentum distributions are quite similar. And no clear momentum dependence of probabilities for kaons and pions faking leptons is observed in this momentum region.

3.6 Results

The ΔM distributions for the muon and electron data and the calculated effective excess of muon fakes over electron fakes are given in Fig. 3.11(a). The histogram is the result of a χ^2 fit of the muon spectrum to the sum of three contributions: the signal, the scaled electrons, and the excess of muon over electron fakes. Here, the sizes of the electron and fake contributions are fixed and only the signal normalization is allowed to vary. We remind the reader that the signal consists of two components, whose relative normalization is fixed. These two components are the decay $D_s^{*+} \to \gamma D_s^+$, $D_s^+ \to \mu^+\nu$ and the direct decay $D_s^+ \to \mu\nu$ and $D^+ \to \mu^+\nu$ combined with a random photon. Our measurement of the D_s^{*+}/D_s^+ production ratio allows us to constrain the relative normalization.

We find a signal of 182$\pm$22 events in the peak which are attributed to the process $D_s^{*+} \to \gamma D_s^+$, $D_s^+ \to \mu^+\nu$. We also find 250$\pm$38 events in the flat part of the distribution corresponding to $D_s^+ \to \mu^+\nu$ or $D^+ \to \mu^+\nu$ decays coupled with a random photon. The contribution of a real $D^+ \to \mu^+\nu$ decay with random photons is not entirely negligible since the $D^{*+} \to \gamma D^+$ branching ratio does not enter. The D^+ fraction is estimated to be about (18$\pm$8)% relative to the total $D_s^+ \to \mu^+\nu$ plus random photon contribution.

To explicitly display the signal, we show, in Fig. 3.11(b), the ΔM distribution after the electrons and the fakes are subtracted. The curve is a fit of the data in Fig. 3.11(a) to the signal shape calculated from the D_s^{*+} sample and random photon background calculated from the D^{*+} sample. All of the events in this plot are signal, the background having already been subtracted.

Using the fit result of 182±22 events, we extract a width for $D_s^+ \to \mu^+\nu$ by normalizing to the the efficiency corrected number of fully reconstructed $D_s^{*+} \to \gamma D_s^+$, $D_s^+ \to \phi\pi^+$ events, 24740±1200±810 [33]. The efficiency for reconstructing the $\phi\pi^+$ decay is obtained from Monte Carlo. We find

$$\frac{\Gamma(D_s^+ \to \mu^+\nu)}{\Gamma(D_s^+ \to \phi\pi^+)} = 0.173 \pm 0.023 \pm 0.035 \quad , \tag{3.8}$$

where the first error is the statistical error on the measured numbers of $\mu^+\nu$ and $\phi\pi^+$ events. The second error is the total systematic error of 18%, whose components are summarized in Table 3.2.

3.6.1 Systematic error and control

Table 3.2: Systematic Errors on Width Ratio (%)

Source of Error	Value	Size of error (%)
Muon fake rate	(0.69±0.05)%	9
Electron fake rate	(0.21±0.03)%	7
$\pi/K/p$ fractions (sources of fakes)	60%/27%/13%	7
μ/e normalization	1.01±0.03	9
Detection efficiency	(4.2±0.3)%	7
D_s^{*+}/D_s^+ production ratio	1.08±0.13	8
$\phi\pi^+$ normalization	24740±1200±810	3
Total systematic error		20

The errors that arise from the relative muon to electron normalization, the muon fake rate, the electron fake rate, and the D_s^{*+}/D_s^+ production ratio, are estimated by fitting the data with each parameter changed by ± 1σ. The error on the relative fractions of pions, kaons and protons entering into the fake rate calculation is computed by changing the fractions to 70%, 20% and 10%, respectively. We judge this to be the outer limit at 90% confidence level of the change possible in these ratios. This, in turn, changes the excess muon to electron to fake rate by 12% leading to a 7% change in the yield. A systematic error of $\pm 3\%$ for the detection efficiency of the normalization mode $\phi\pi^+$ is also included.

3.6.2 Radiative leptonic decay contribution

The radiative decay rates for $D_s^+ \to \ell^+\nu\gamma$ and $B^+ \to \ell^+\nu\gamma$ have been considered by Burdman, Goldman and Wyler [9]. They predict that

$$\frac{\Gamma(D_s^+ \to \mu^+\nu\gamma)}{\Gamma(D_s^+ \to \mu^+\nu)} = (1 - 10) \times 10^{-2}\mu_V^2 \text{ GeV}^2, \tag{3.9}$$

where μ_V^2 is a vector coupling constant which has a value of approximately 0.1 for the D_s^+ meson. While the radiative decay rate for B^+ is comparable to the non-radiative rate, the radiative decay rate for D_s^+ is estimated to be between 0.1% and 1% of the non-radiative rate. Furthermore, they also predict that the radiative muon and electron rates are equal, so our electron subtraction would remove any residual effect.

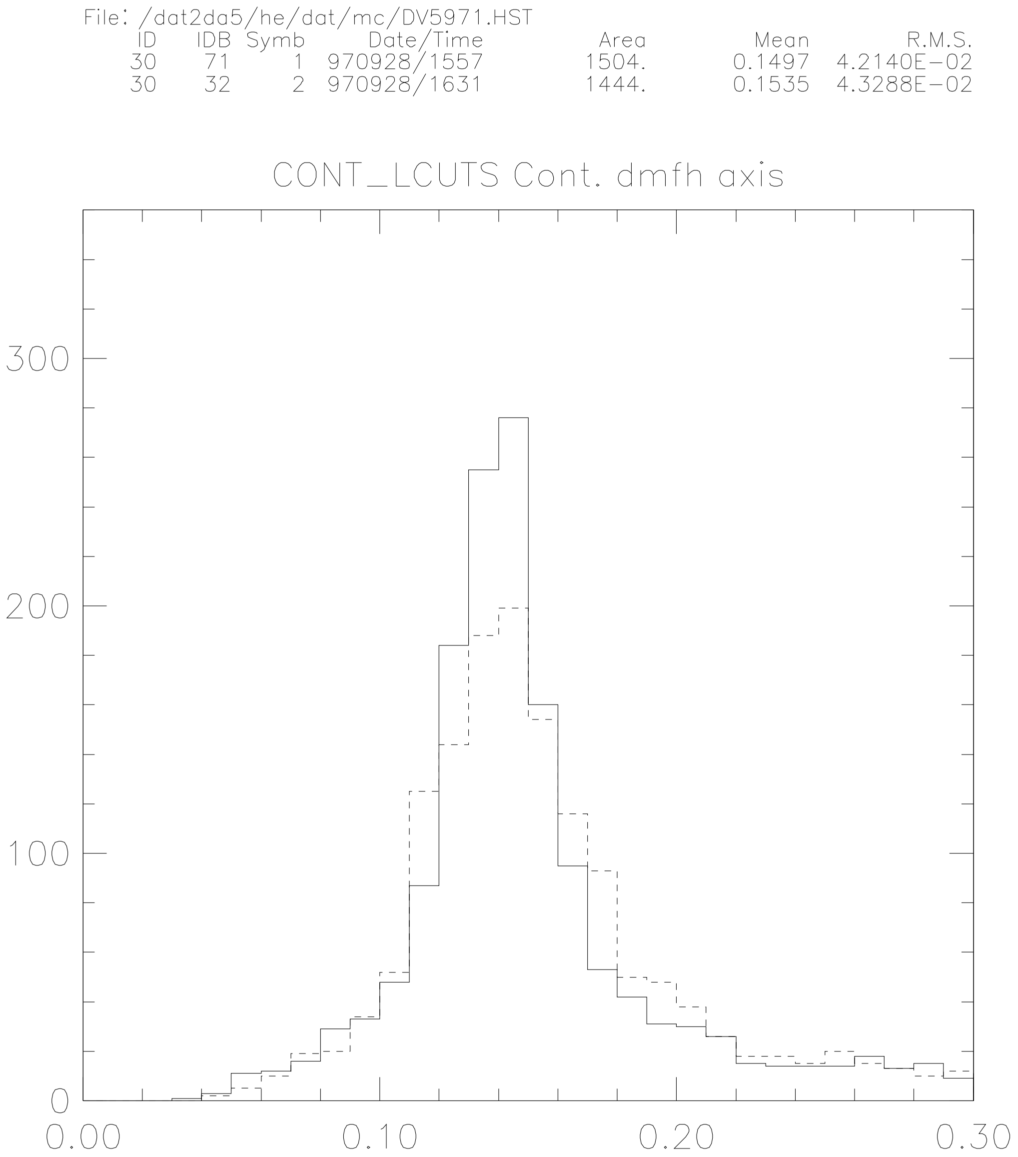

Figure 3.1: ΔM distribution for $D_s^{*+} \to D_s^+\gamma, D_s^+ \to \mu\nu$ event Monte Carlo. Solid line is from using the new D_s^+ mass constrained correction technique, dashed line is from the old method.

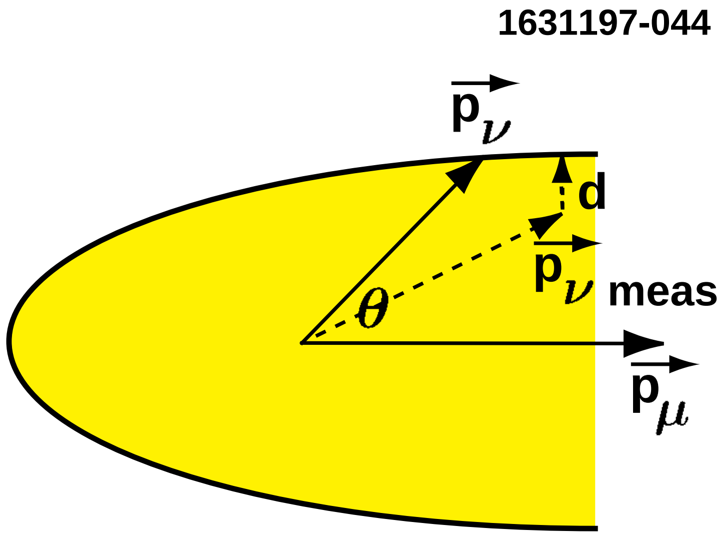

Figure 3.2: The relationship between the muon and neutrino momentum vectors and the constraint surface imposed by the D_s invariant mass.

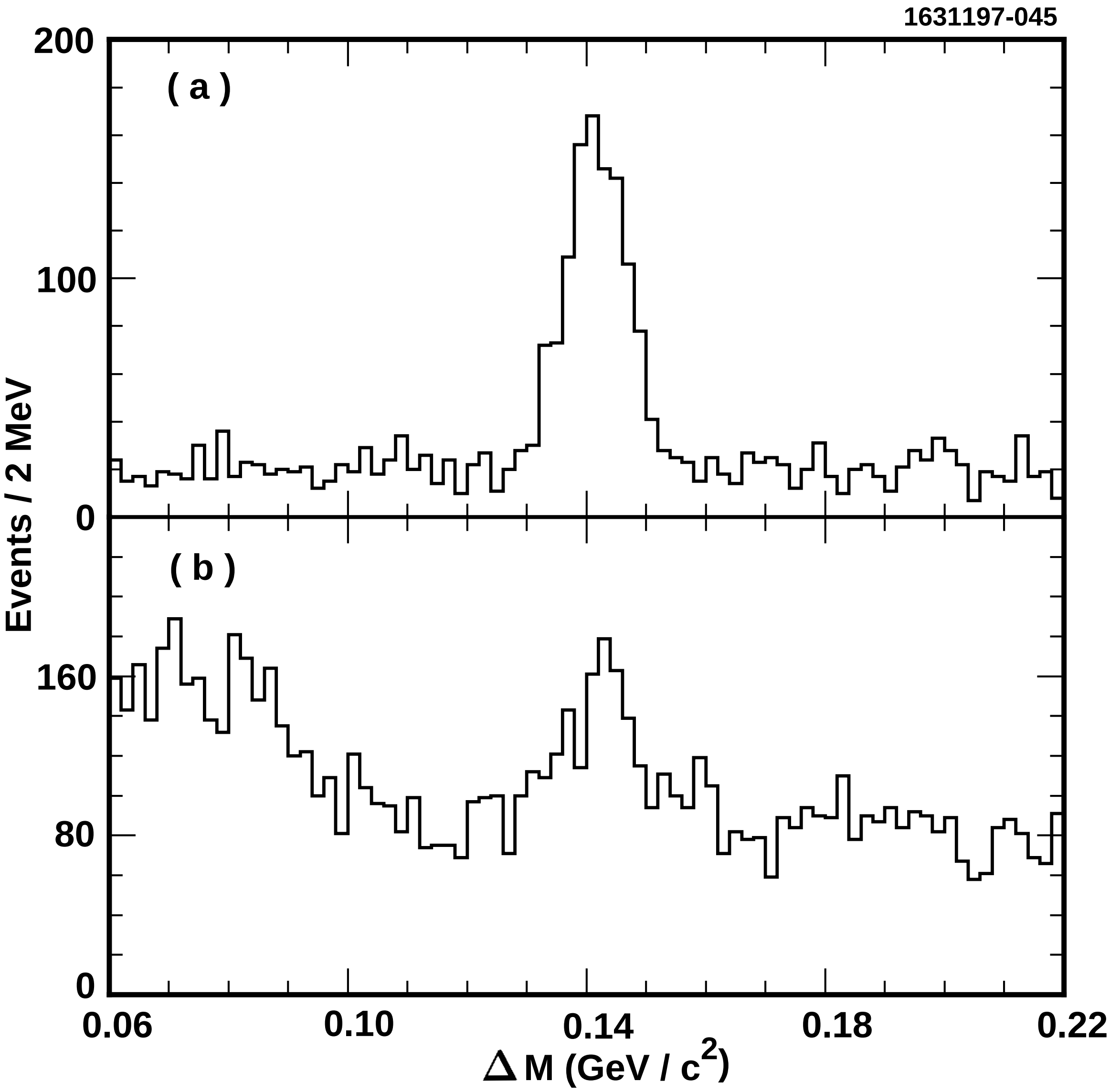

Figure 3.3: The $\Delta M = M(\gamma K^-\pi^+) - M(K^-\pi^+)$ mass difference distributions for fully reconstructed events of $D^{*o} \to \gamma D^o$, $D^o \to K^-\pi^+$, after a requirement that the $K^-\pi^+$ mass be within 2.5 standard deviations of the D^o mass. (a) D^{*o} Monte Carlo (b) data.

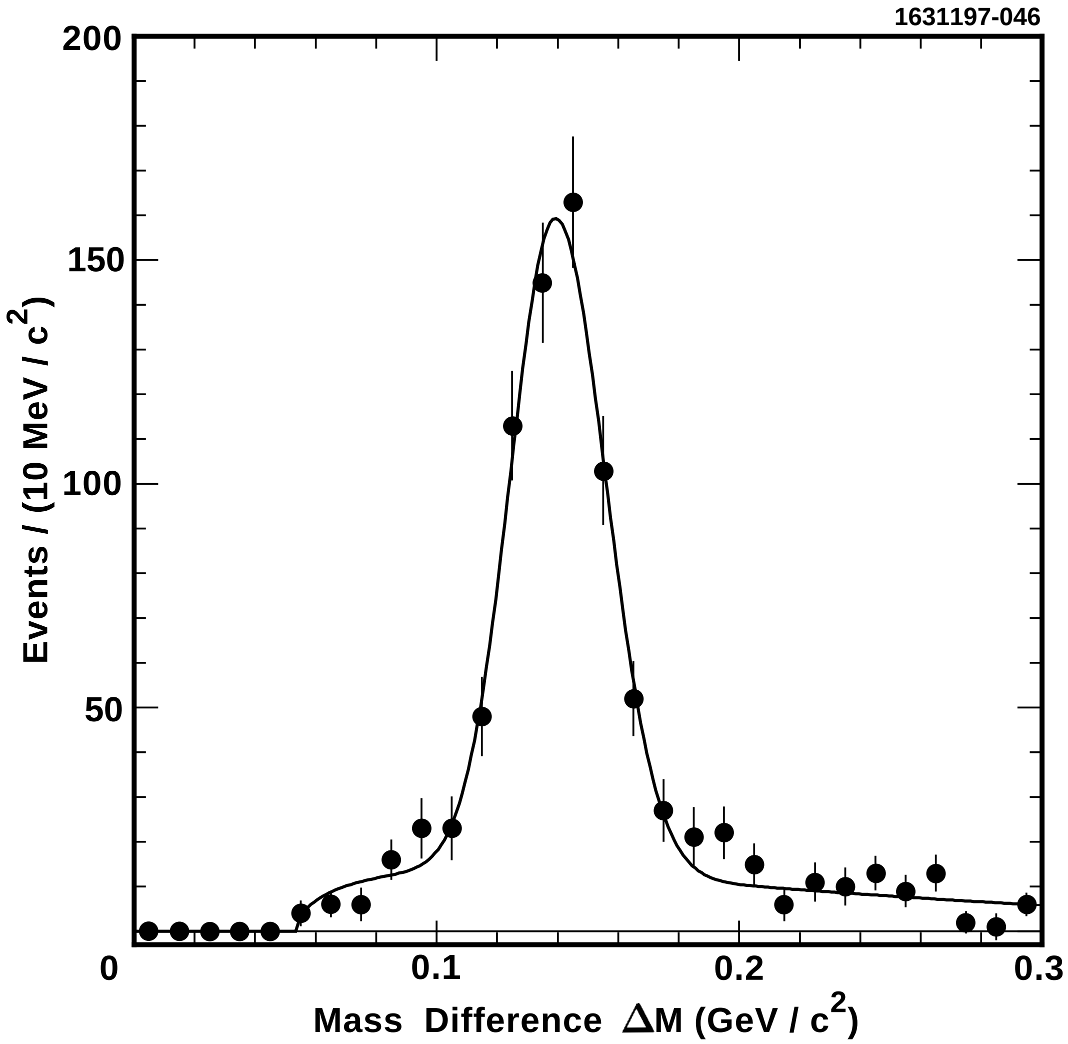

Figure 3.4: The $\Delta M = M(\gamma K p_{miss}) - M(K p_{miss})$ mass difference distributions for the simulated missing momentum analysis using Monte Carlo of $D^{*o} \to \gamma D^o$, $D^o \to K^-\pi^+$. A sideband subtraction to remove background in the initial D^{*o} selection has been applied. The curve and fitting procedure are described in the text.

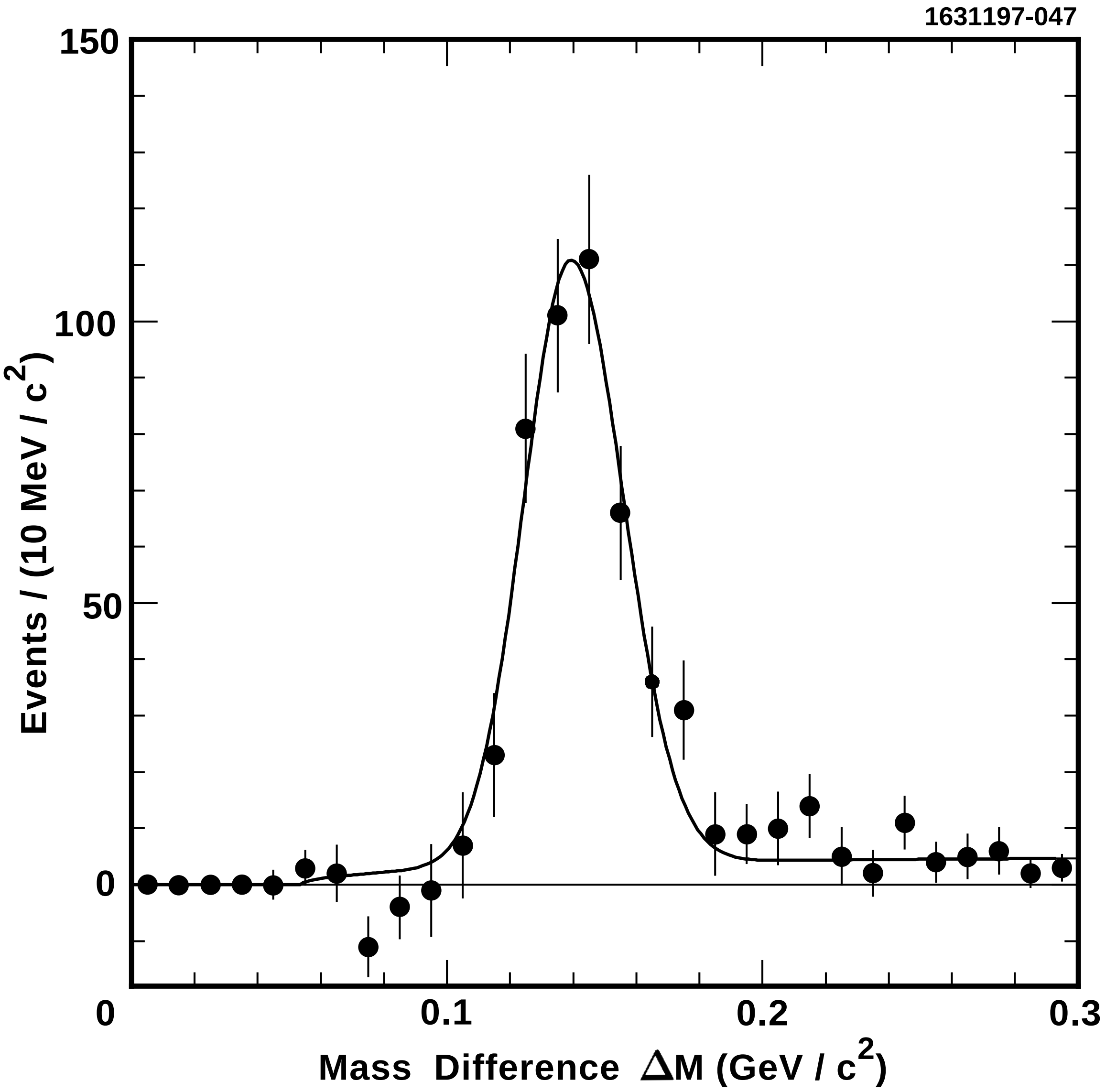

Figure 3.5: The $\Delta M = M(\gamma K p_{miss}) - M(K p_{miss})$ mass difference distributions for the simulated missing momentum analysis for the $D^{*o} \to \gamma D^o$, $D^o \to K^- \pi^+$ real data. A sideband subtraction to remove background in the initial D^o selection has been applied. The curve used is from the Monte Carlo signal shape.

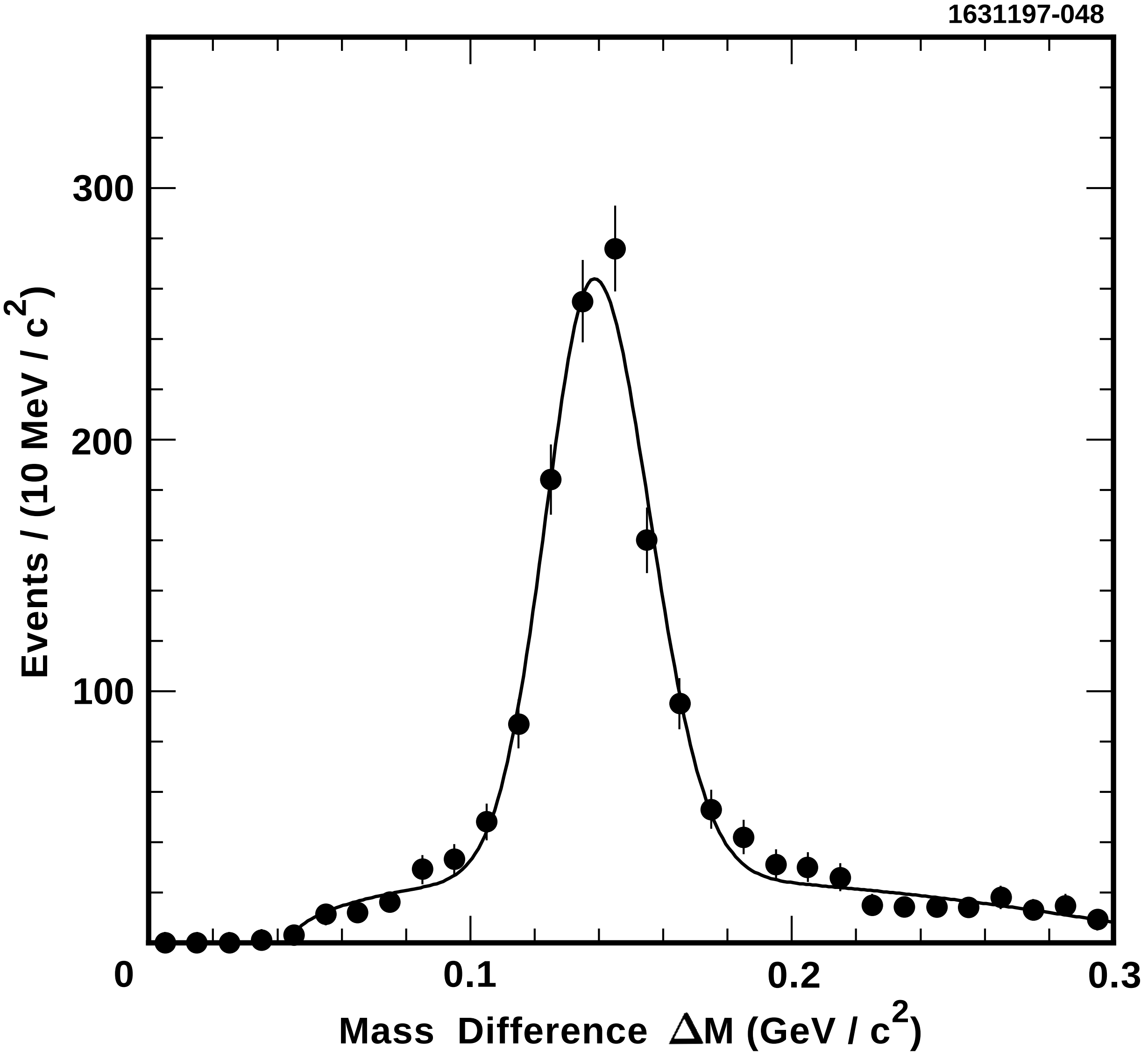

Figure 3.6: The $\Delta M = M(\gamma\mu p_{miss}) - M(\mu p_{miss})$ mass difference distributions for the missing momentum analysis for the $D_s^{*+} \to \gamma D_s^+$, $D_s^+ \to \mu^+\nu$ Monte Carlo. The curve and fitting procedure are described in the text.

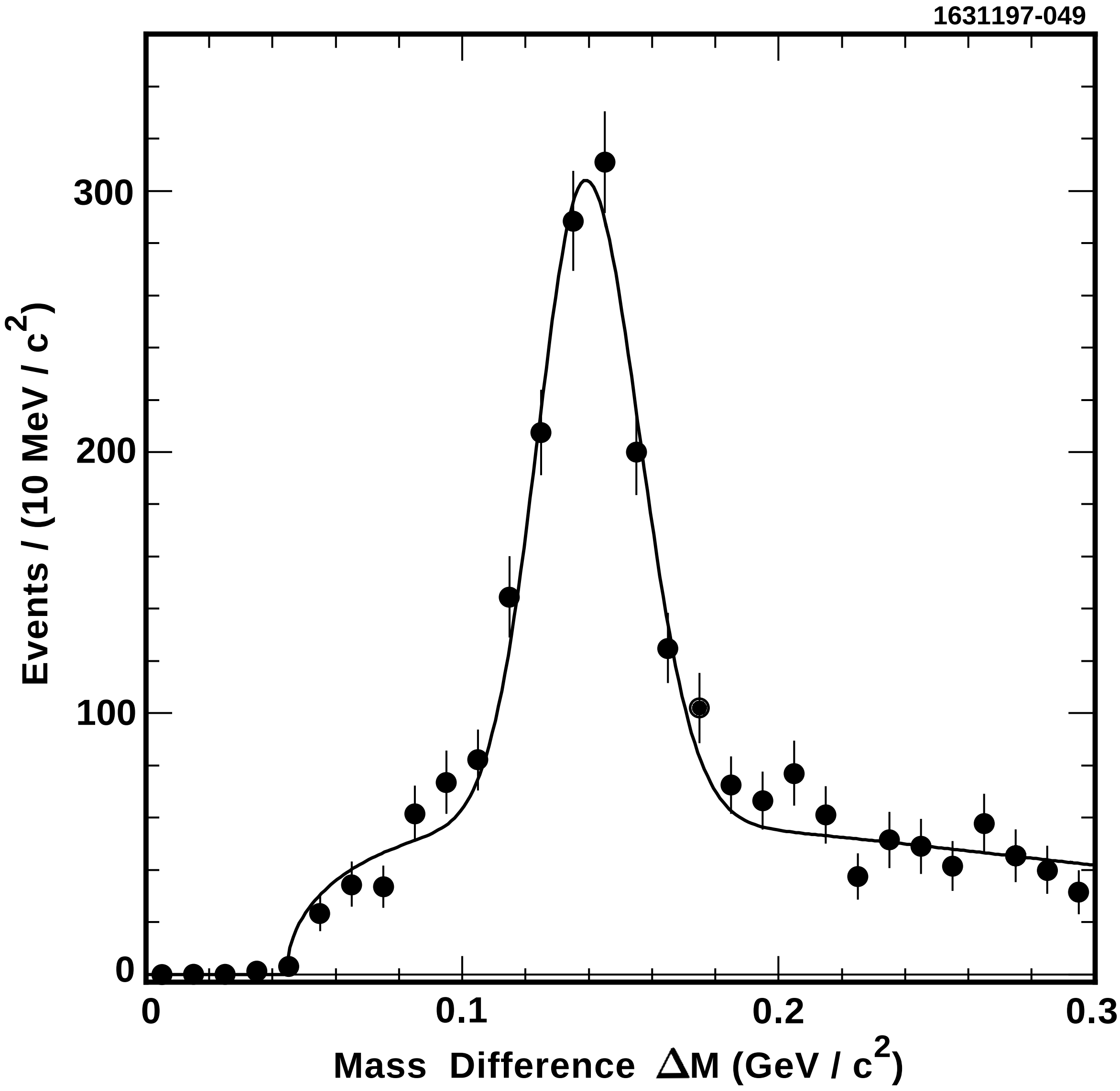

Figure 3.7: The $D_s^{*+} \rightarrow \gamma D_s^+$, $D_s^+ \rightarrow \mu^+\nu$ signal distribution plus random photon background as determined from the signal Monte Carlo simulation combined with the D^{*+} data sample analyzed for the missing ν as $D^{*o} \rightarrow \gamma D^o$, $D^o \rightarrow K^- p_{miss}$. The curve is a fit using the functions described in the text.

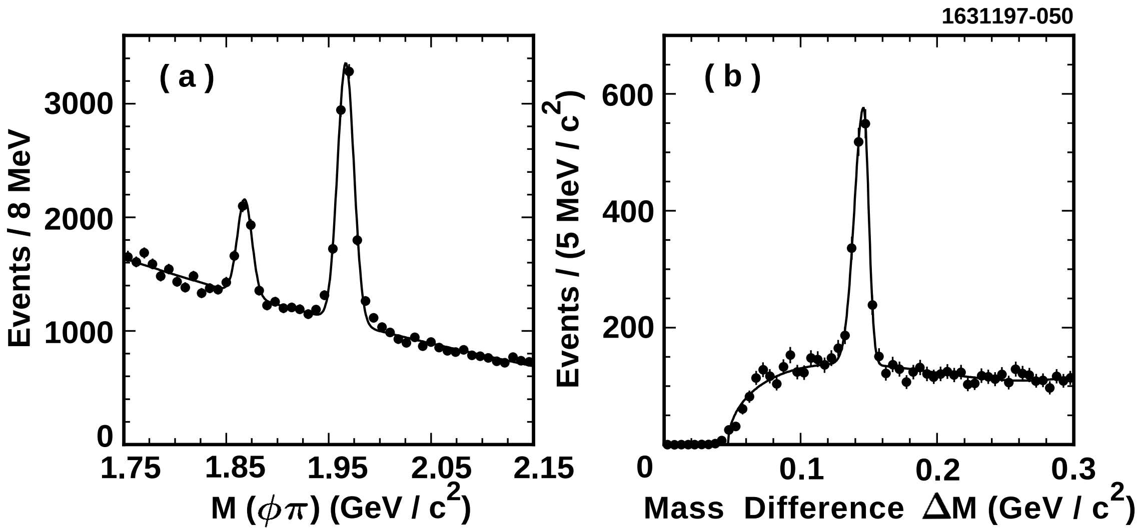

Figure 3.8: (a) The $\phi\pi^+$ mass distribution and (b) the $\Delta M = M(\gamma\phi\pi^+) - M(\phi\pi^+)$ mass difference distribution with the requirement that $\phi\pi^+$ mass is consistent with the known D_s^+ mass. The signal shapes are taken from Monte Carlo simulation. The background shape in (a) is a second order polynomial, while in (b) it is the sum of half-integer polynomials.

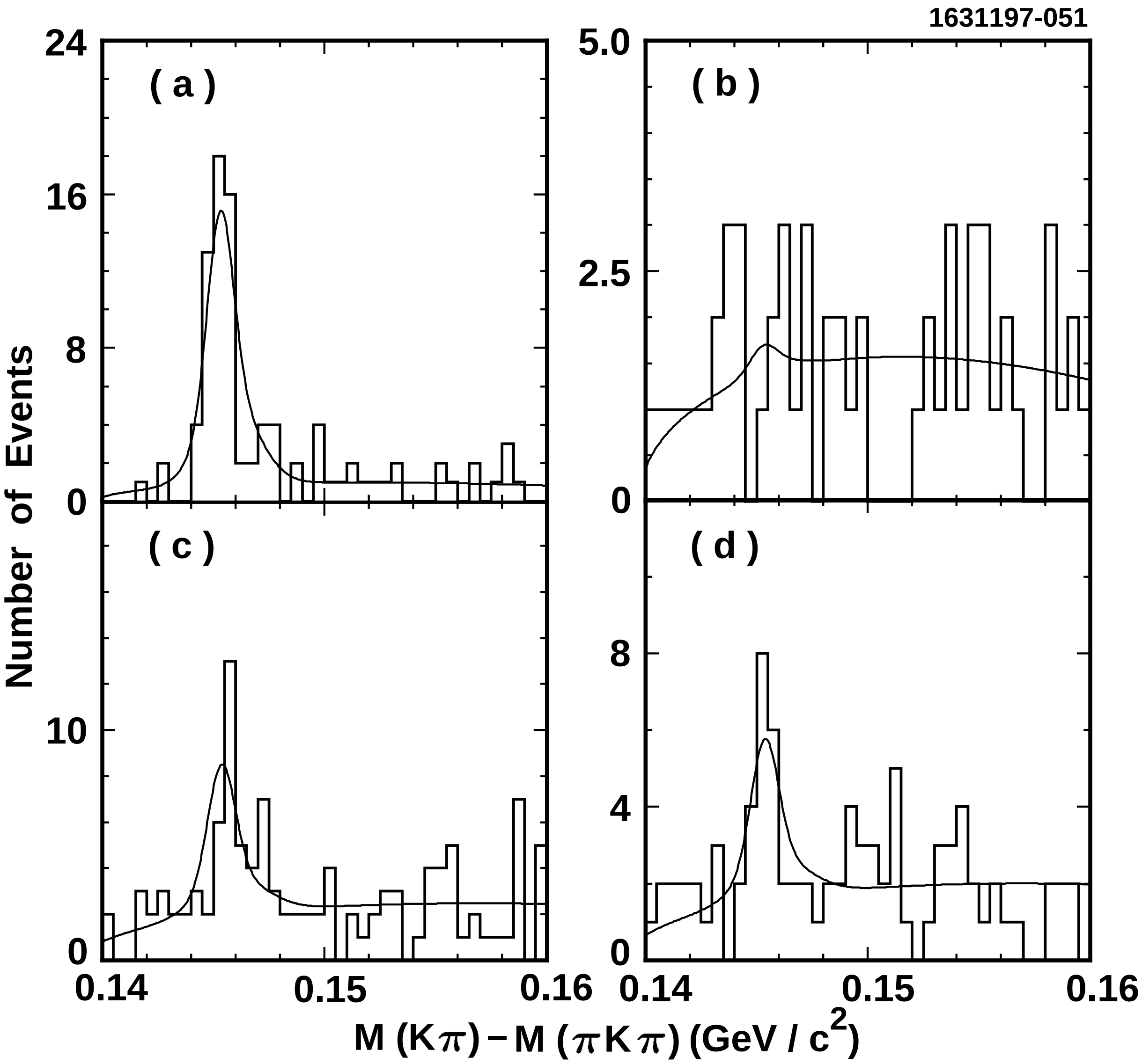

Figure 3.9: $M(\pi K\pi) - M(K\pi)$ mass difference distributions for four cases of hadrons identified as leptons: (a) kaon as muon, (b) kaon as electron, (c) pion as muon, (d) pion as electron. The signal shapes were determined from the distribution of mass difference for fully reconstructed D^{*+} candidates. The area of the Gaussian component and the normalization of the background are allowed to float.

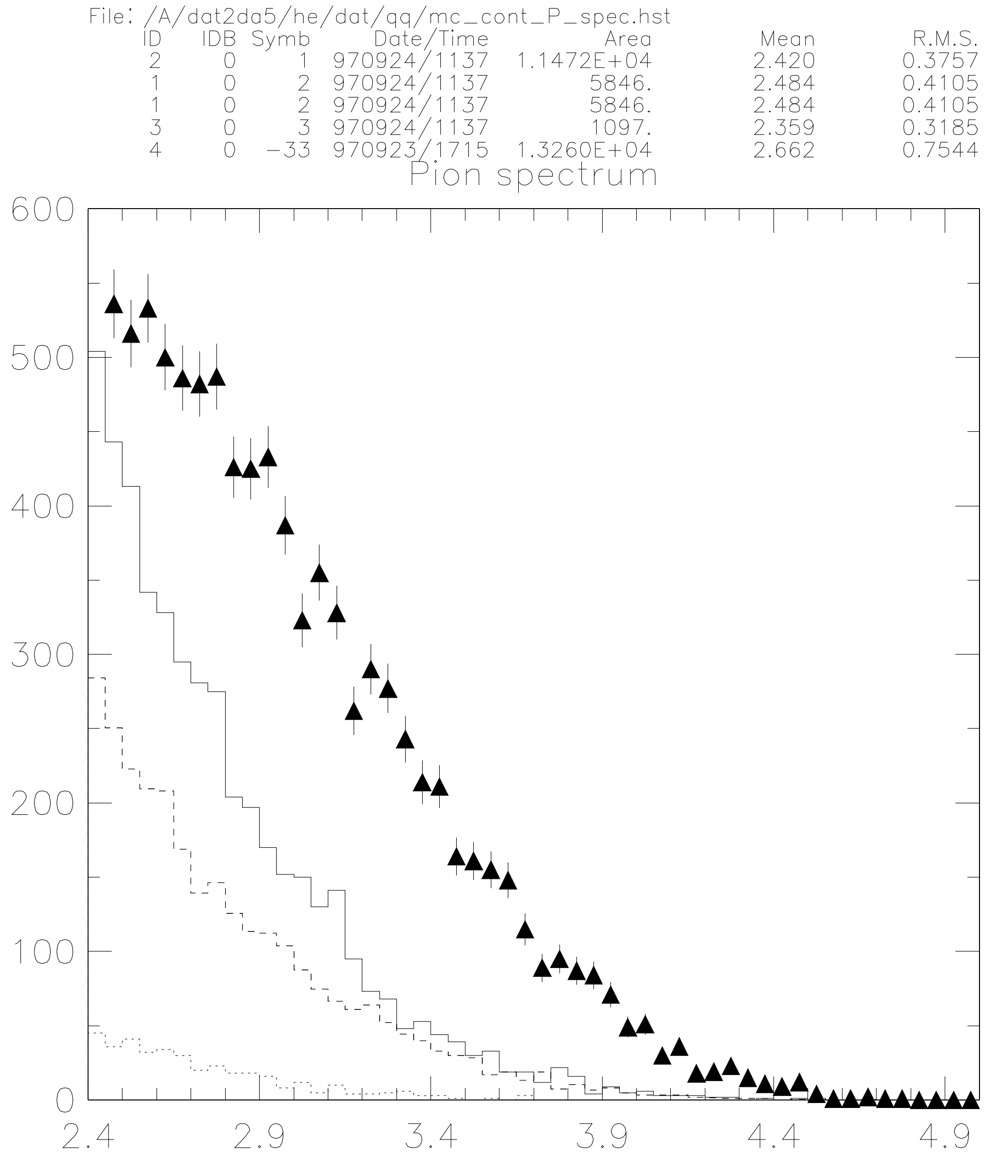

Figure 3.10: Momentum distribution of hadron track candidates from Monte Carlo which pass all of our cuts and would enter into the ΔM signal region if they were identified as muons. Shown here are pions (solid line), kaons(dashed line) and protons (dotted line). Also shown as solid triangle is the distribution of muons coming from $D_s^+ \to \mu^+\nu$ which should be the same with the kaon and pion distribution coming from the D^{*+} samples that we used for fake rate determination.

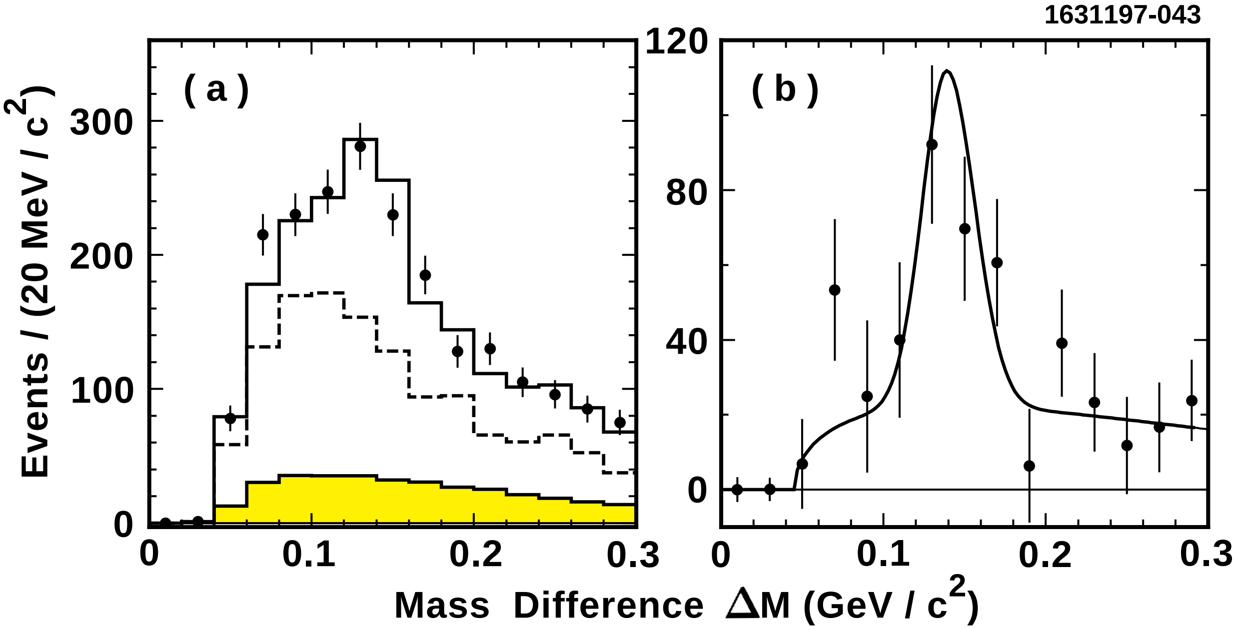

Figure 3.11: (a) The ΔM mass difference distribution for D_s^{*+} candidates for both the muon data (solid points), the electron data (dashed histogram) and the excess of muon fakes over electron fakes (shaded). The histogram is the result of the fit described in the text. (b) The ΔM mass difference distribution for D_s^{*+} candidates with electrons and excess muon fakes subtracted. The curve is a fit to the signal shape described in the text.

Chapter 4

Summary

4.1 Conclusions

We have measured the ratio of decay widths

$$\Gamma(D_s^+ \to \mu^+\nu)/\Gamma(D_s^+ \to \phi\pi^+) = 0.173 \pm 0.023 \pm 0.035 \quad . \tag{4.1}$$

To extract the decay constant f_{D_s} we need to known the partial width for the $D_s^+ \to \phi\pi^+$ decay. The total D_s^+ width is well known because of precise lifetime measurements [15], but the absolute $\phi\pi^+$ branching ratio has a large error. Using the latest PDG average value $\mathcal{B}(D_s^+ \to \phi\pi^+)$ of (3.6±0.9)%, and $\tau_{Ds} = (4.67 \pm 0.17) \times 10^{-13}$s, we find

$$f_{D_s} = (280 \pm 19 \pm 28 \pm 34) \text{ MeV} \quad . \tag{4.2}$$

The first error is statistical, and the second is systematic resulting from our relative width ratio measurement, and the third error reflects the uncertainty in the absolute $D_s^+ \to \phi\pi^+$ branching ratio. This result supersedes our previous one, using a data sample that includes the one used in the previous analysis. The reduction in the central value is primarily due to the better measurement of the lepton fake rates that lowered the pion/electron fake rate.

For comparison, we list in Table 4.1 the old CLEO result and published results from other experiments that used the $D_s^+ \to \mu^+\nu$ decay to measure f_{D_s}. We have changed the values of f_{D_s} according to the new PDG D_s decay branching fractions for the normalization modes [35], and have corrected the old CLEO result by using the new fake rates determined in this analysis [17]. The lowering of the central value of the old CLEO result is mostly due to the change in the fake rate determination, which is now much more precise.

Table 4.1: Current Experimental Results on f_{D_s} Using $D_s^+ \to \mu^+\nu$

Collaboration	Observed Events	Published f_{D_s} value (MeV)	Corrected f_{D_s} value (MeV)
CLEO (old) [16]	39±8	$344 \pm 37 \pm 52 \pm 42$	$282 \pm 30 \pm 43 \pm 34$
WA75 [17]	6	$232 \pm 45 \pm 20 \pm 48$	$213 \pm 41 \pm 18 \pm 26$
BES [18]	3	$430^{+150}_{-130} \pm 40$	Same
E653 [19]	$23.2 \pm 6.0^{+1.0}_{-0.9}$	$194 \pm 35 \pm 20 \pm 14$	$200 \pm 35 \pm 20 \pm 26$
CLEO (this work)	182±22	-	$280 \pm 19 \pm 28 \pm 34$

In addition, there are new results using the $D_s^+ \to \tau^+\nu$ decay from the L3 collaboration [36] of $309 \pm 58 \pm 33 \pm 38$ MeV, and 330 ± 95 from the DELPHI collaboration [37]. Our new measurement gives the most accurate of f_{D_s}. The world average value for f_{D_s} is $(255 \pm 21 \pm 28)$ MeV, where the common systematic error is due the error on the absolute branching ratio for $D_s^+ \to \phi\pi^+$.

Theoretical predictions of f_{D_s} have been made using many methods. Recent lattice gauge QCD calculations [38] give central values of 199 to 221 MeV with quoted errors in the ±40 MeV range. C. Bernard's new world average for lattice theory calculations gives 221±25 MeV.[39]

Other theoretical estimates use potential models whose values [40] range from 210 to 356 MeV, and QCD sum rule estimates [41] that are between 200 and 290 MeV. Predictions for f_{D_s} have also been made by combining theory with experimental input. Assuming factorization for $\overline{B} \to D^* D_s^-$ decays combined with measured branching ratios, gives a value of f_{D_s} range of about 280 MeV with an error of about 60 MeV[42]. Use of experimental data on isospin mass splittings in the D^* and D system gives a value for f_D of 290 MeV [43]. (f_{D_s} is thought to be 10% to 20% higher than f_D).

4.2 Future improvement prospect

After the CESR luminosity upgrade and installation of CLEO III detector, $\Gamma(D_s^+ \to \mu^+\nu)/\Gamma(D_s^+ \to \phi\pi^+)$ and the Pseudoscalar Decay Constant f_{Ds} measurement will be greatly improved.

The high luminosity will improve the statistical error by an order of magnitude to the 1% level. But to really achieve the model discrimination power, systematic error control is the most important.

The availability of RICH particle ID information will help to improve this measurement in two ways, better neutrino reconstruction resolution and better hadron/lepton fake control.

Neutrino reconstruction resolution is better because we can accurately judge charged particle mass when summing up the 4-vectors to do missing momentum calculation. Whereas now, every charged track is assumed to be pion unless it is positively identified s kaon or proton. The discriminating power for particle ID is very poor for particles above 800 MeV.

Secondly with RICH, we'll have better $K/e, K/\mu, \pi/e$ discrimination for energetic tracks, although it won't affect π/μ fake rate because their mass is so close. This will substantially reduce the systematic effect of hadron/lepton fakes.

With more data, we are also going to have better fake rate, and normalization measurements. And we can afford to suppress the background further by cutting harder on missing momentum and applying other cuts like total missing charge and total lepton number, which we omitted here to increase efficiency.

Appendix I–List of cuts used

- "Class 10" event
- TRKMNG check for all charged tracks and SPLITF check for all γ's
- Lepton ID: MUDPTH ≥ 7 for muon, R2ELEC ≥ 3 for electron
- Track quality cuts for the lepton candidate:
  - KINCD ≥ 0
  - RESICD ≤ 0.4 mm
  - $|$DBCD$| \leq 2$ mm
  - $|$Z0CD$| \leq 50$ mm
  - RHITDR ≥ 0.4 .and. NPT +NVD ≥ 5

    where RHITDR is the ration of actual numbers of hits (i.e. layers) over the expected number of hits per track in the main drift chamber DR, and NPT and NVD are the number of hits per track in the PT and VD, respectively
- $P_{lepton} \geq 2.4$ GeV
- $cos\theta_{lepton} \leq 0.85$
- $E_\gamma \geq 150$ MeV
- "Standard Good Gamma" cuts, good barrel region only, and π^0 veto
- $P_{miss} \geq 0.8$ GeV
- $\mid m^2_{miss} \mid \leq 2.0$ GeV^2
- $cos\theta_{miss} \leq 0.9$

- 1.2 GeV $\leq m_{D_s} \leq$ 3.0 GeV
- $P_{D_S^*} \geq$ 2.4 GeV
- Photon angle cut and thrust angle cut (see text)

Bibliography

[1] L. Montanet *et. al.* Review of Particle Properties. *Phys. Rev. D*, 50(3):1173-1826, 1994.

[2] N. Cabibbo, *Phys. Rev. Lett.* 10, 531 (1963); M. Kobayashi and K. Maskawa *Prog. Theor. Phys.* 49, 652 (1973).

[3] L. Wolfenstein *Phys. Rev. Lett.* 51, 1945 (1983).

[4] Sheldon Stone, "The Goals and Techniques of BTeV and LHC-B", presented at "Heavy Flavor Physics: A Probe of Nature's Grand Design" , Varenna, Italy, July 1997.

[5] M. Gaillard and B. Lee, *Phys. Rev.* D10, 897, (1974); J. Hagelin, *Phys. Rev.* D20, 2893, (1979); A. Ali and A. Aydin, *Nucl. Phys.* B148, 165 (1979); T. Brown and S. Pakvasa, *Phys. Rev.* D31, 1661, (1985); S. Pakvasa, *Phys. Rev.* D28, 2915, (1985); I. Bigi and A. Sanda, *Phys. Rev.* D29, 1393, (1984).

[6] C. Zeitnitz, "Oscillations and Mixing," presented at BEAUTY 96.

[7] A. J. Buras, "Theoretical Review of B-physics," in **BEAUTY '95** ed. N. Harnew and P. E. Schlein, *Nucl. Instr. and Meth.* A368, 1 (1995).

[8] M. Suzuki (Lawrence Berkeley Lab), Phys. Rev. **D50**, 1443 (1994).

[9] G. Burdman, T. Goldman and D. Wyler, Phys. Rev. D **51**, 111 (1995).

[10] M. Acciarri *et al.* (L3 Collaboration), Phys. Lett. B **396**, 327 (1997)

[11] M. Artuso *et al.* (CLEO Collaboration), Phys. Rev. Lett. **75**, 785 (1995).

[12] A. Sokolov and G.C. Zucchelli (DELPHI), submitted to XXIX Int. Conf. on High Energy Physics, Vancou ver, Canada, July 1998 paper ICHEP98 242 (1998); ALEPH collaboration, Paper submitted to Int. Conf on HEP, Warsaw PA10-019 (1996).

[13] J. L. Rosner, in **Particles and Fields 3**, Proceed. of the 1988 Banff Summer Inst., Banff, Alberta, Canada, ed. by A. N. Kamal and F. C. Khanna, World Scientific, Singapore, 1989, 395.

[14] Whenever a specific reaction or final state is mentioned, consideration of the charge conjugate reaction or final state is also implied.

[15] R.M. Barnett *et al.*, (Particle Data Group), Phys. Rev. D **54**, 1 (1996).

[16] D. Acosta *et al.*, Phys. Rev. **D49**, 5690 (1994).

[17] S. Aoki *et al.*, Progress of Theoretical Physics **89**, 131 (1993). The WA75 value was based on the 1992 PDG value of $\mathcal{B}(D_s^+ \to K^+K^-\pi^+) = (3.9 \pm 0.4)\%$ and $\mathcal{B}(D^o \to \mu\nu X) = (8.8 \pm 2.5)\%$. We scale the WA75 result to be $f_{D_s} = (238 \pm 47 \pm 21 \pm 43)$MeV using updated PDG [15] values of $\mathcal{B}(D_s^+ \to K^+K^-\pi^+) = (4.8 \pm 0.7)\%$ and $\mathcal{B}(D^o \to e\nu X) = (7.7 \pm 1.2)\%$ which we use for $\mathcal{B}(D^o \to \mu\nu X)$, after reducing the value by 3% to account for the smaller muon phase space.

[18] J. Z. Bai *et al.*, Phys. Rev. Lett. **74**, 4599 (1995).

[19] K. Kodama *et al.*, Phys. Lett. **B382** 299 (1996).

[20] Y. Kubota *et al.*, (CLEO Collaboration), Nucl. Instrum. Methods Phys. Res., Sec. A **320**, 66 (1992).

[21] Y. Kubota et al., (CLEO Collaboration). The CLEO-II detector. *Nuclear Instruments & Methods in Physics Research*, A 320:66–113, 1992.

[22] F. Würthwein and J. Alexander. Momentum Resolution at 2.6 GeV/c. CLEO internal note, CBX 93-39.

[23] C.J.Bebek *et al.* Nucl. Inst. Meth. A302, 261 (1991)

[24] S. Sanghera., A Measurement of Hadronic Cross Section at CLEO and a Test of QCD, CLEO internal note, CBX 95-38.

[25] D. Besson and Ina Robertin. Preliminary Note on R. CLEO internal note, CBX 95-70.

[26] JETSET 7.3, T.Sjöstrand and M. Bengtsson, Comput. Phys. Commun. **43**, 367 (1987)

[27] GEANT – Detector Description and Simulation Tool, 1993.

[28] M. S. Alam *et al.* (CLEO Collaboration), "The Observation of the Radiative Decay $D^{*+} \to D^+\gamma$," CONF 96-7, ICHEP-96 PA01-80 (1996).

[29] D. Atwood and W. Marciano, Phys. Rev. **D41**, 1736 (1990).

[30] To use our $D^{*+} \to \pi^+ D^o$, $D^o \to K^-\pi^+$ events here, we eliminate the measurements of the fast π^+ from the D^o decay from both the tracking chambers and calorimeter to simulate the neutrino, and call the K^- a muon.

[31] The event sample used is the fully reconstructed sample of D^{*o} events, $D^{*o} \to \gamma D^o$, $D^o \to K^-\pi^+$, with the K^- required to have momentum above 2.4 GeV/c.

[32] To compare with the efficiency in the $D_s^+ \to \mu^+\nu$ channel, the muon identification effiency of 0.85 must be taken into account, yielding an overall efficiency of 4.1%.

[33] The efficiencies quoted here are both for $\phi\pi^+$ momenta above 2.4 GeV/c. To calculate the $D_s^{*+} \to \gamma D_s^+$, $D_s^+ \to \phi\pi^+$ yield above 2.4 GeV/c D_s^{*+} momentum, we remove the cut on the $\phi\pi^+$ momentum and impose a cut on the D_s^{*+} momentum.

[34] The CLEO Collaboration is preparing a publication on the measurement of the vector/pseudoscalar ratio in charmed-strange mesons.

[35] C. Caso *et al.*, The European Physics Journal, **C3** 1, 1998.

[36] M. Acciarri *et al.* (L3 Collaboration), Phys. Lett. B **396**, 327 (1997).

[37] F. Parodi *et al.* (DELPHI Collaboration), "Measurement of the Branching Fraction $D_s^+ \to \tau^+\nu_\tau$," DELPHI 97-105 CONF 87, submitted to HEP'97 Conference Jerusalem, August 1997, paper 455.

[38] See C. Bernard,"Lattice Calculations of Decay Constants," review talk presented at the Seventh International Symposium on Heavy Flavor Physics, Santa Barbara, July 7-11, 1997, hep-ph/9709460, and references cited therein; A. X. El-Khadra *et al.*, "B and D Meson Decay Constants in Lattice QCD," hep-ph/9711426 (1997).

[39] C. Bernard, "Lattice Calculations of Decay Constants," in proceedings of 7th Int. Symp on Heavy Flavor Physics, Santa Barbara (1997).

[40] H. Krasemann, Phys. Lett. B **96**, 397 (1980); M. Suzuki, Phys. Lett. B **162**, 391 (1985); S. Godfrey and N. Isgur, Phys. Rev. D **32**, 189 (1985); S. N. Sinha, Phys. Lett. B **178**, 110 (1986); P. Cea *et al.*, Phys. Lett. B **206**, 691 (1988); S. Capstick and S. Godfrey, Phys. Rev. D **41**, 2856 (1988).

[41] C. Dominguez and N. Paver, Phys. Lett. B **197**, 423 (1987); S. Narison, Phys. Lett. B **198**, 104 (1987); L. J. Reinders, Phys. Rev. D **38**, 947 (1988); M. A. Shifman, Usp. Fiz. Nauk **151**, 193 (1987) [Sov. Phys. Usp. **30**, 91 (1987)].

[42] D. Bortoletto and S. Stone, Phys. Rev. Lett. **65**, 2951 (1990); J. L. Rosner, Phys. Rev. D **42**, 3732 (1990); H. Albrecht *et al.* (ARGUS Collaboration), Zeit. Phys. C **54**, 1 (1992); T. Browder, K. Honscheid and S. Playfer, "A Review of Hadronic and Rare B Decays," in B **Decays** 2nd edition, ed. S. Stone, World Scientific, Singapore, p 158 (1994).

[43] J. F. Amundson *et al.*, Phys. Rev. D **47**, 3059 (1993).

BIOGRAPHICAL SKETCH

The author, Weipin He, was born in Beijing, P.R.China on December 4th, 1967. He graduated with a B.S. degree in physics from Peking University, Beijing, P.R.China in 1990. He worked for the Institute of Biophysics, Academy of Science of China in Beijing through Aug. 1990 to June, 1991. Then he joined the experimental High Energy Physics group in Syracuse University as a research assistant in August, 1991 He worked in Wilson lab of Cornell University as a visiting student during summer and fall of 1993.